A computational fluid dynamics—Population balance equation approach for evaporating cough droplets transport

Original
A computational fluid dynamics—Population balance equation approach for evaporating cough droplets transport / Feng, Y.i., Li, D., Marchisio, D., Vanni, M., Buffo, A.. - In: INTERNATIONAL JOURNAL OF MULTIPHASE FLOW. - ISSN 0301-9322. - 165:(2023), pp. 1-18. [10.1016/j.ijmultiphaseflow.2023.104500]

Publisher:
Elsevier

Published
DOI:10.1016/j.ijmultiphaseflow.2023.104500

Highlights

A computational fluid dynamics - population balance equation approach for evaporating cough droplets transport

Yi Feng,Dongyue Li,Daniele Marchisio,Marco Vanni,Antonio Buffo

- The Eulerian-Eulerian approach is coupled with the population balance equation to trace the evolution of respiratory droplets
- Sectional method and quadrature based moment method are used to solve the population balance equation
- The CFD-PBE approach can be used to trace the size changes of evaporating droplets, the evolution of exhaled breathe and the particle dispersion in 3D chamber
- The CFD-PBE approach is applied in the dispersion of polydisperse evaporating cough droplets in a 3D chamber

A computational fluid dynamics - population balance equation approach for evaporating cough droplets transport

Yi Feng[a], Dongyue Li[b], Daniele Marchisio[a], Marco Vanni[a] and Antonio Buffo[a,*]

[a] *Politecnico di Torino, Corso Duca degli Abruzzi 24, Torino, 10129, Italy*
[b] *DYFLUID Ltd, Beijing, 100029, P.R. China*

ARTICLE INFO

Keywords:
Eulerian-Eulerian approach
Population balance equation
Respiratory droplets
COVID-19

ABSTRACT

Airborne diseases, including COVID-19, are transmitted by respiratory droplets, which makes the study of the evolution of these droplets important to control the transmission. However, the evolution of the droplets is complex, being a multiphase, polydisperse, multicomponent system undergoing evaporation. To numerically investigate such multiphase flows, there are mainly two approaches. One is the Eulerian-Lagrangian (E-L) approach, which is widely used due to its ability to trace the dispersion and evaporation of individual droplets. However, this approach generally has high costs and difficulty in post-processing. The other one is the Eulerian-Eulerian (E-E) approach, which, though having lower costs, is less adopted because of its failure to treat the features of polydispersity and evaporation. In order to take advantage of the low-costs of E-E approach, the population balance equation (PBE) is combined with the E-E approach to trace the polydisperse evaporating droplets. Two PBE solving methods, sectional method (SM) and quadrature based moment method (QBMM), are used and compared. The codes are developed based on the OpenFOAM library and their abilities to predict size changes of evaporating droplets, evolution of expelled airflow front, and aerosols concentration are assessed by using the experimental and numerical results in literature. Good agreements with the reported results are found, indicating the reliability of the CFD-PBE approaches. The SM and QBMM are finally applied in the transport of cough droplets in a 3D chamber. The suspending trends of small droplets and the falling trends of the large droplets are obtained by both methods. The droplets are found to be able to travel a distance longer than 2 m, which is valuable for the guidelines of social distancing. Additionally, the advantages and disadvantages of SM and QBMM are discussed.

1. Introduction

Some infectious diseases, such as COVID-19, can be transmitted by the expelled virus-laden droplets, known as droplets transmission or airborne transmission (WHO, 2020). Therefore, the knowledge about the transport of the virus-laden droplets expelled during respiratory activities is of great importance for breaking the transmission chain and controlling infection.

However, the evolution of the expelled droplets is complex, holding the feature of multiphase, polydisperse, multicomponent and evaporation (Balachandar et al., 2020). During respiratory activities, such as speaking, coughing or sneezing, the respiratory droplets containing water and a dry solid nucleus made by non-volatile substances (Liu and Duan, 2012) will be expelled together with the exhaled breath (i.e. in gaseous phase) from the mouth or nose. The droplets are carried by and interact with the exhaled breath. For the cough droplets, their velocities can reach up to 22 $\mathrm{m \cdot s^{-1}}$ (Zhu et al., 2006), and their sizes can vary from micrometers to millimeters (Chao et al., 2009). Furthermore, the droplets will evaporate. As a result, the varied velocities and sizes will not only affect the transmission but also affect the evaporation rate (Wei and Li, 2015), changing the droplet behavior in space and time. Literature shows that 100 μm is an important threshold (Wells (1934) and Mittal et al. (2020)): the larger droplets (>100 μm) usually cannot fully evaporate, so they will settle on the ground within certain distance due to gravity, showing a ballistic trajectory. The smaller droplets (<100 μm), on the contrary, can quickly evaporate into droplets of few micrometers, and thus suspending in the air for longer times and transported for longer distances. Furthermore, both the exhaled droplets and breath consist of multiple components, which will affect the dispersion and evaporation of the respiratory droplets through relative humidity (Li et al., 2018) and non-volatile substances (Li et al., 2020).

---

[*] Corresponding author

yi.feng@polito.it (Y. Feng); li.dy@dyfluid.com (D. Li); daniele.marchisio@polito.it (D. Marchisio); marco.vanni@polito.it (M. Vanni); antonio.buffo@polito.it (A. Buffo)
ORCID(s):

To study the evolution of the respiratory droplets, experiments concerning different aspects were carried out. Burgmann and Janoske (2021) experimentally analyzed the aerosols transmission (0.3-10 μm) in a classroom equipped with air purifier system by measuring the aerosols concentration at different locations. The results indicated that the air purifier system could significantly reduce the aerosols concentration at certain locations. Zhang et al. (2021) studied the transmission of non-evaporating aerosols (5 nm to 10 μm) generated by a smoke generator in a bus. The influence of the location on the bus and the effects of having windows open or closed were assessed. They found that opening windows could significantly reduce the aerosols concentration. Similarly, Ooi et al. (2021) studied the aerosols transmission (1 μm) in a double-decker bus. Experiments for different activities (coughing and talking mimicked by smoke generator) with or without mask under working air-conditioning systems were performed. It was found that the air-conditioning system could greatly influence the dispersion of aerosols and thus increase infection risk of certain seats. And wearing a mask could significantly reduce the relative aerosol concentration of surrounding seats. Wang et al. (2022a) adopted the water tunnel to investigate the cough droplets dispersion from a person going up- or downstairs. Detailed velocities measurements and flow visualization were conducted. It was found that going upstairs makes particles concentrating below the person's shoulder with short downward moving distance while going downstairs causes the particle dispersing over the person's head with long transmission distance. Coldrick et al. (2022) studied the dispersion and deposition of respiratory emissions generated during a series of real activities in an unventilated chamber. The experiment showed a great deposition of bacteria within 1m of the subject. Meanwhile, the exhaled microorganisms could also travel 2 m and remain suspended in the air within a room. Stiehl et al. (2022) used the particle imaging velocimetry (PIV) to studies the evolution of aerosols and droplets expelled during a human sneeze. They extracted the sneeze emission concentration at 0.6 m and 0.9 m away from the mouth and found that maximal concentration is found in region slightly lower than the mouth at 0.6 m. These studies shed light on the droplets and aerosols transmission and reveal the influencing factors. However, due to the limitation of experimental technologies, some details and mechanisms of the droplets transmissions still need to be revealed.

Fortunately, computational fluid dynamics (CFD) provides a fast and reliable tool to predict the evolution of the respiratory droplets. For the multiphase flows of the droplets dispersion, there are mainly two approaches (Capecelatro and Desjardins, 2013). One approach is the Eulerian-Lagrangian (E-L) approach, which tracks the motion of each individual droplet. This approach can easily treat droplet polydispersity and evaporation. Therefore, the E-L approach is widely used in the dispersion and evaporation of respiratory droplets. To accurately capture the flow characteristics, some researchers adopted the direct numerical simulation (DNS) to model the Eulerian field of the E-L approach. Rosti et al. (2020) adopted DNS and E-L approach to investigate the effect of different relative humidities and initial size distributions on dispersion and virus load of the cough droplets. They found that these two factors affected the final size distribution through evaporation and thus resulting in different dispersion pattern and virus load. Wang et al. (2021b) investigated the motion and evaporation of droplets in a turbulent jet-spray using DNS and E-L approach. They found that the higher Reynolds number will result in longer evaporation length due to a lower average vaporization rate. Chong et al. (2021) employed DNS and Lagrangian statistics to study the effect of turbulence and relative humidity on the lifetime of small droplets. It was found that both factors can significantly extend the lifetime of droplets. The effect of turbulence is further revealed by Rosti et al. (2021). They found that the turbulent fluctuations of the supersaturation field are the root cause of the extended droplets lifetime. Additionally, Fabregat et al. (2021a) used DNS to investigate the flow field of a mild cough. Later, they coupled DNS with E-L to investigate the dispersion and evaporation of cough droplets, where the map of virus load and the number of virus copies per inhalation were presented (Fabregat et al., 2021b).

Considering the possible high computational costs, the Reynolds-averaged Navier–Stokes (RANS) equations are widely adopted for the gas phase in more complex scenarios, such as elevator (Sen, 2021), airplane cabin zone (Talaat et al., 2021), classroom (He et al., 2021), restaurant (Liu et al., 2021), bus (Yang et al., 2022) and ship (Huang et al., 2022). In particular, Dbouk and Drikakis (2020) used E-L approach to studied the cough droplets transport, where the effects of relative humidity, evaporation and wind speed etc. were taken into account. They found that increasing wind speed, the droplets can be transported for a longer distance (up to 6 m) though with decreasing concentration and sizes. Feng (2020) numerically investigated the effect of wind speed and relative humidity (RH) on cough droplets transport. They found the similar influence of the wind speed. It was also found that high RH could result in droplets growth and thus promote droplets deposition. Li et al. (2020) simulated the cough droplets dispersion in a tropical outdoor environment with the E-L approach. In addition to the influence of RH, wind speed and social distancing, they also paid attention to the effects of droplet compositions on evaporation rate. They found that salt water droplets had lower evaporation rate than pure water droplets, indicating that considering droplet compositions is necessary in the simulation of actual respiratory droplets. Li et al. (2021) studied the dispersion of cough droplets from a passenger riding an escalator. It was found that the movement of the coughing passenger could significantly affect the flow field of expelled puff and the dispersion of droplets. On a descending escalator, the droplets had a higher suspending height and a larger spreading range. Motamedi et al. (2022) numerically investigated the speaking droplets dispersion in confined space under different ventilation strategies. They found that different ventilation strategies generated diverse background flow fields and thus affecting the droplets dispersion. Suitable ventilation strategies could reduce droplets concentration. These studies using E-L approach revealed important influencing factors in the dispersion and evaporation of respiratory droplets, presenting the advantages and disadvantages of this approach (Garg et al. (2009), Salman and Soteriou (2004) and Li et al. (2015)).

Another possible approach is the Eulerian-Eulerian (E-E) framework. This approach treats the disperse phase as a continuum, therefore it has lower costs and advantages in post-processing. Different simplified E-E approach have already been applied in gas-particle flows in indoor environments, such as single fluid model (or passive-scalar model) (Zhang and Chen, 2007) and mixture model (Chen et al. (2006) and Zhao et al. (2008)). Diwan et al. (2020) adopted DNS to study the evolution of the cough or sneeze flows without droplets. In their later works, they coupled E-E approach with DNS to investigate the dispersion of small cough droplets (10 μm) (Singhal et al., 2021) and the virus transmission during short conversations (Singhal et al., 2022). For RANS method, Yan et al. (2020) compared the two-fluid model (TFM), one kind of E-E approach, with E-L approach in their study on the transport of non-evaporating aerosols (0.2, 0.77 and 2.5 μm) in a ventilated room. They found that the two approaches had similar accuracy in predicting the airflow field. And they thought the E-E approach had advantages in providing a mechanistic description of the inter-phase interactions, while the E–L approach had advantage in modelling particle–wall interactions. Pei et al. (2021) adopted the TFM to study the aerosols transmission in a ventilated room, where two sizes (1 and 10 μm) of non-evaporating aerosols were considered. It was found that the buoyancy-driven flows could lead to a longer transmission distance and higher infection risk. Zhang et al. (2021) investigated the aerosols transmission in a bus where the passive-scalar model was used to trace the evolution of aerosols concentration. It was found that suitable ventilation systems, opening windows and doors, and wearing masks could significantly reduce the concentration. Wang et al. (2022b) coupled the Wells-Riley model with the passive-scalar model to estimate the infection probability in a ventilated train. They also found that importance of ventilation system and wearing masks for reducing infection risk. From these studies, it can be noted that the E-E approach are mainly used in aerosols transmission where the aerosols are of small sizes, monodisperse and non-evaporating. This is because the E-E approach is hard to treat polydispersity and evaporation (Shiea et al., 2020). Therefore, this approach is less used in the dispersion and evaporation of respiratory droplets. Considering its advantages in low costs and complexity, developing new methods based on the E-E approach is still prospective.

The objective of this study is to develop a flexible, robust, and computationally cheap tool based on the E-E approach to investigate the dispersion and evaporation of polydisperse respiratory droplets. To this end, the population balance equation (PBE) is introduced. The PBE is a continuity statement written in terms of the droplet number density function (NDF), and is able to provide a detailed description of the disperse phase (Marchisio and Fox, 2013). In recent year, the PBE has been coupled with TFM and applied in polydisperse bubble flows with (Lehnigk et al., 2022) or without (Heylmun et al., 2019) interphase mass transfer. Satisfactory performances are observed. However, up to the authors' knowledge, this coupled approach has not been applied in the study of respiratory droplets transport. Therefore, a CFD-PBE coupled approach capable of tracing the dispersion and evaporation of the polydisperse respiratory droplets will be presented in this study. Two different PBE solving methods, sectional method (SM) and quadrature-based moment method (QBMM), will be investigated based on the open-source software OpenFOAM. To assess the reliability of the two methods, they will be verified and validated against the experimental or numerical results concerning different aspects of respiratory droplets transport in literature.

This paper is arranged as follows: Section 2 presents the two-fluid model, population balance modelling and the coupling method. Section 3 presents the validation and the application of the CFD-PBE approach. The evaporation model will be validated first using the reported results of the evaporation of a single droplet and the freely falling droplets. Then, the CFD-PBE approach will be validated with the experimental results of the jet front evolution of a sneeze, and the aerosols transmission in a ventilated chamber. Eventually, the approach will be applied in the transport of cough droplets in a three-dimensional chamber. Some conclusions are drawn in Section 4.

2. Methodology

2.1. Multi-fluid model: transport of mass, momentum and heat

2.1.1. Governing equations

The multiphase system of the respiratory droplets is generally dilute, owning a low disperse phase volume fraction (Chao et al., 2009). However, considering the small sizes of the droplets, there are usually enough droplets so that the continuum assumption of E-E approach always holds. When the multi-fluid model (MFM), one E-E approach, is applied to the droplets, the disperse liquid phase is described by the superposition of a number of pseudo-phases made of droplets of different diameter d_d. Each pseudo-phase is treated as a continuum in the model, so that the governing equations for the dth disperse pseudo-phase can be written as:

$$\frac{\partial}{\partial t}(\alpha_d \rho_d) + \nabla \cdot (\alpha_d \rho_d \mathbf{U}_d) = \dot{m}_{\mathrm{c}d} - \dot{m}_{d\mathrm{c}}, \tag{1}$$

$$\frac{\partial \alpha_d \rho_d \mathbf{U}_d}{\partial t} + \nabla \cdot (\alpha_d \rho_d \mathbf{U}_d \otimes \mathbf{U}_d) = -\alpha_d \nabla p + \nabla \cdot (\alpha_d \mathbf{R}_{\mathrm{Eff},d}) + \alpha_d \rho_d \mathbf{g} + \mathbf{M}_d + (\dot{m}_{\mathrm{c}d} \mathbf{U}_\mathrm{c} - \dot{m}_{d\mathrm{c}} \mathbf{U}_d), \tag{2}$$

$$\begin{aligned} \frac{\partial}{\partial t} \left(\alpha_d \rho_d \left(E_d + K_d\right)\right) + \nabla \cdot \left(\alpha_d \rho_d \mathbf{U}_d \left(E_d + K_d\right)\right) =& \nabla \cdot (\alpha_d a_{\mathrm{Eff},d} \nabla E_d) - \alpha_d \nabla \cdot (p \mathbf{U}_d) + \alpha_d \rho_d \mathbf{g} \cdot \mathbf{U}_d \\ &+ (Q_{\mathrm{fd},d} + \dot{m}_{\mathrm{fd},d} E_{\mathrm{fd},d} + \dot{m}_{\mathrm{c}d} K_\mathrm{c} - \dot{m}_{d\mathrm{c}} K_d), \end{aligned} \tag{3}$$

where the subscript c represents the continuous phase, d is the index of the disperse phase and f represents the interface between the continuous and the disperse phase. Therefore, α_d, ρ_d and $\mathbf{U}_d$ are the disperse phase volume fraction, density and velocity, respectively. The interphase mass transfer rate per unit volume for condensation and evaporation are $\dot{m}_{\mathrm{c}d}$ and $\dot{m}_{d\mathrm{c}}$, respectively; they are non-negative and become equal to 0 when there is no condensation or evaporation. The pressure p is shared by the continuous and disperse phase. The term $\mathbf{R}_{\mathrm{Eff},d}$ is the effective stress tensor containing laminar and turbulent contribution; $\mathbf{g}$ is the gravitational acceleration vector; $\mathbf{M}_d$ is the interfacial force term; E_d is the sensible internal energy and K_d is the kinetic energy; $a_{\mathrm{Eff},d}$ is the effective thermal diffusivity; $Q_{\mathrm{fd},d}$ and $\dot{m}_{\mathrm{fd},d}$ are the heat and mass flux from the interface into the dth disperse phase, respectively; $E_{\mathrm{fd},d}$ is the sensible internal energy of the dth disperse phase under the temperature of the interface, and consequently, $\dot{m}_{\mathrm{fd},d} E_{\mathrm{fd},d}$ represents the energy transfer from the interface to the dth disperse phase caused by the mass transfer.

In most cases, we will use only one disperse phase, so that the approach reduces to the two-fluid model (TFM), but sometimes, we will need to include in the model two disperse phases of different sizes, d_1 and d_2, and solve a real MFM. In the latter case, however, we will neglect the interfacial transfer terms (of mass, momentum and heat) between the disperse phases and only include the terms between each single disperse phase and the continuous phase ; indeed, the systems we will study are quite dilute with no coalescence or breakup, and thus we can assume that all interfacial transfer processes are mediated by the continuous phase.

For the continuous phase, the volume fraction can be calculated using $\alpha_\mathrm{c} = 1 - \sum_d \alpha_d$. Similarly, continuity, momentum and energy equations can be written as:

$$\frac{\partial}{\partial t}(\alpha_\mathrm{c} \rho_\mathrm{c}) + \nabla \cdot (\alpha_\mathrm{c} \rho_\mathrm{c} \mathbf{U}_\mathrm{c}) = \sum_d \left(\dot{m}_{d\mathrm{c}} - \dot{m}_{\mathrm{c}d}\right), \tag{4}$$

$$\frac{\partial \alpha_\mathrm{c} \rho_\mathrm{c} \mathbf{U}_\mathrm{c}}{\partial t} + \nabla \cdot (\alpha_\mathrm{c} \rho_\mathrm{c} \mathbf{U}_\mathrm{c} \otimes \mathbf{U}_\mathrm{c}) = -\alpha_\mathrm{c} \nabla p + \nabla \cdot (\alpha_\mathrm{c} \mathbf{R}_{\mathrm{Eff,c}}) + \alpha_\mathrm{c} \rho_\mathrm{c} \mathbf{g} - \sum_d \mathbf{M}_d + \sum_d \left(\dot{m}_{d\mathrm{c}} \mathbf{U}_d - \dot{m}_{\mathrm{c}d} \mathbf{U}_\mathrm{c}\right), \tag{5}$$

$$\begin{aligned} \frac{\partial}{\partial t} \left(\alpha_\mathrm{c} \rho_\mathrm{c} \left(E_\mathrm{c} + K_\mathrm{c}\right)\right) + \nabla \cdot \left(\alpha_\mathrm{c} \rho_\mathrm{c} \mathbf{U}_\mathrm{c} \left(E_\mathrm{c} + K_\mathrm{c}\right)\right) =& \nabla \cdot (\alpha_\mathrm{c} a_{\mathrm{Eff,c}} \nabla E_\mathrm{c}) - \alpha_\mathrm{c} \nabla \cdot (p \mathbf{U}_\mathrm{c}) + \alpha_\mathrm{c} \rho_\mathrm{c} \mathbf{g} \cdot \mathbf{U}_\mathrm{c} \\ &+ \sum_d (Q_{\mathrm{fc},d} + \dot{m}_{\mathrm{fc},d} E_{\mathrm{fc},d} + \dot{m}_{d\mathrm{c}} K_d - \dot{m}_{\mathrm{c}d} K_\mathrm{c}). \end{aligned} \tag{6}$$

In the simulations discussed later, the turbulent or the laminar flow assumption, depending on the flow features, will be used for the continuous phase whereas the laminar assumption will be used for the disperse phase in all cases. For the turbulent continuous phase, RNG $k-\epsilon$ model will be used.

Considering the evaporation, the continuous (gas) phase consists of two components, the water vapor and the dry air. Therefore, only the water vapor transport equation is required to characterize composition:

$$\frac{\partial}{\partial t}(\alpha_c \rho_c Y_{H_2O}) + \nabla \cdot (\alpha_c \rho_c \mathbf{U}_c Y_{H_2O}) - \nabla \cdot (\alpha_c D_{\mathrm{Eff,c}} \nabla Y_{H_2O}) = \sum_d \left(\dot{m}_{dc} - \dot{m}_{cd} \right), \tag{7}$$

where Y_{H_2O} is the water vapor mass fraction in the gas phase and $D_{\mathrm{Eff,c}}$ is the effective diffusivity.

2.1.2. Interfacial force term

In the dispersion of respiratory droplets, particle weight and drag are largely predominant over the other forces, which are consequently neglected in most of the literature. In the momentum equations (see Eq. (2) and Eq. (5)), droplet weight is considered through the gravity term, and the drag force is included in the interfacial force term:

$$\mathbf{M}_d = \mathbf{F}_{\mathrm{D},d} = \frac{3}{4} C_{\mathrm{D}} \mathrm{Re} \frac{\alpha_d \rho_c \nu_c}{d_d^2} (\mathbf{U}_c - \mathbf{U}_d), \tag{8}$$

where C_{D} is the drag coefficient, d_d is the dth disperse phase diameter, ν_c is the continuous phase kinematic viscosity, $\mathrm{Re} = d_d |\mathbf{U}_c - \mathbf{U}_d| / \nu_c$ is the relative Reynolds number. C_{D} can be calculated as (Schiller and Naumann, 1933):

$$C_{\mathrm{D}} = \begin{cases} \frac{24}{\mathrm{Re}} \left(1 + 0.15\mathrm{Re}^{0.687}\right), & \mathrm{Re} \le 1000; \\ 0.44, & \mathrm{Re} > 1000. \end{cases} \tag{9}$$

Also for the drag coefficient, the system can be assumed to be dilute and the drag coefficient can be assumed to be that of an isolated droplet.

2.1.3. Interfacial mass transfer

The mass transfer rate of water per unit volume between the continuous phase and the dth disperse phase (or in the dth interface), $\dot{m}_d$, can be calculated as:

$$\dot{m}_d = \rho_c k_d (Y_{\mathrm{f},d} - Y_{H_2O}), \tag{10}$$

where k_d is the volumetric mass transfer coefficient in the dth interface, $Y_{\mathrm{f},d}$ and Y_{H_2O} are the water vapor mass fraction in the dth interface and the gas phase, respectively. When $\dot{m}_d \ge 0$, evaporation happens and thus $\dot{m}_{dc} = \dot{m}_d$ and $\dot{m}_{cd} = 0$. When $\dot{m}_d < 0$, condensation happens and thus $\dot{m}_{cd} = -\dot{m}_d$ and $\dot{m}_{dc} = 0$.

The volumetric mass transfer coefficient in the dth interface, k_d, can be calculated as:

$$k_d = \frac{6\alpha_d \mathrm{Sh} D_c}{d_d^2}, \tag{11}$$

where D_c is the molecular diffusivity, and the Sherwood number is calculated using the Frössling equation as: $\mathrm{Sh} = 2 + 0.552\mathrm{Re}^{1/2}(\mathrm{LePr})^{1/3}$ (Frössling, 1938). In this equation, $\mathrm{Le} = a_c / D_c$ is the Lewis number defined as the ratio of thermal diffusivity $a_c = \kappa_c / (\rho_c C_{p,c})$ to mass diffusivity D_c, and $\mathrm{Pr} = \nu_c / a_c$ is the Prandtl number defined as the ratio of momentum diffusivity (kinetic viscosity) ν_c to thermal diffusivity a_c. It should be noted that only the volumetric mass transfer coefficient on the continuous phase side is required, because the disperse phase (droplets) is assumed to consist of pure water offering no resistance.

The mass fraction of vapor at the dth interface, $Y_{\mathrm{f},d}$, is obtained by the saturation model as:

$$Y_{\mathrm{f},d} = \frac{M_i}{M} \frac{p_{\mathrm{Sat},d}}{p}, \tag{12}$$

where M_i is the molecular weight of water, M is the average molecular weight of the gas phase, and $p_{\mathrm{Sat},d}$ is the saturation pressure at the dth interface under interfacial temperature $T_{\mathrm{f},d}$ and can be obtained by the Antoine equation as:

$$p_{\mathrm{Sat},d} = \exp\left(A + \frac{B}{C + T_{\mathrm{f},d}} \right), \tag{13}$$

where $A = 23.952$, $B = -4233.7$ and $C = -31.737$ (Li et al., 2018).

2.1.4. Interfacial heat transfer

The two-resistance model is adopted here to better consider the heat transfer process with different heat transfer coefficients on the two sides of the dth interface and to obtain $T_{\mathrm{f},d}$. At the dth interface, $T_{\mathrm{f},d}$ is assumed to be identical on both sides. Therefore, the heat fluxes $Q_{\mathrm{fd},d}$ and $Q_{\mathrm{fc},d}$ can be calculated as:

$$Q_{\mathrm{fd},d} = h_{\mathrm{d},d}(T_{\mathrm{f},d} - T_d), \tag{14}$$

$$Q_{\mathrm{fc},d} = h_{\mathrm{c},d}(T_{\mathrm{f},d} - T_{\mathrm{c}}), \tag{15}$$

where $h_{\mathrm{d},d}$ and $h_{\mathrm{c},d}$ are the volumetric heat transfer coefficients in the dth interface of the disperse phase side and continuous phase side, respectively; T_d and T_{c} are the phase temperatures. The coefficient $h_{\mathrm{c},d}$, describing the turbulent heat transfer from the surface of a sphere to the surrounding fluid, can be calculated as:

$$h_{\mathrm{c},d} = \frac{6\alpha_d \kappa_{\mathrm{c}} \mathrm{Nu}}{d_d^2}, \tag{16}$$

where κ_{c} is the continuous phase thermal conductivity. The Nusselt number Nu is obtained from the Ranz-Marshall correlation as $\mathrm{Nu} = 2 + 0.6\mathrm{Re}^{1/2}\mathrm{Pr}^{1/3}$ (Ranz and Marshall (1952a); Ranz and Marshall (1952b)). The coefficient $h_{\mathrm{d},d}$, describing the heat transfer from the surface of a sphere to the fluid within the sphere, can be calculated as:

$$h_{\mathrm{d},d} = \frac{60\alpha_d \kappa_{\mathrm{c}}}{d_d^2}. \tag{17}$$

Since neither mass nor heat can be stored at the dth interface, the mass and heat balance at the interface can be written as follows:

$$\begin{cases} \dot{m}_{\mathrm{fd},d} + \dot{m}_{\mathrm{fc},d} = 0, \\ (Q_{\mathrm{fd},d} + \dot{m}_{\mathrm{fd},d} E_{\mathrm{fd},d}) + (Q_{\mathrm{fc},d} + \dot{m}_{\mathrm{fc},d} E_{\mathrm{fc},d}) = 0. \end{cases} \tag{18}$$

Since $\dot{m}_{\mathrm{fd},d} = -\dot{m}_d$,

$$h_{\mathrm{d},d}(T_{\mathrm{f},d} - T_d) + h_{\mathrm{c},d}(T_{\mathrm{f},d} - T_{\mathrm{c}}) = \dot{m}_{\mathrm{fd},d}(E_{\mathrm{fc},d} - E_{\mathrm{fd},d}) = -\dot{m}_d L_d, \tag{19}$$

where $L_d = E_{\mathrm{fc},d} - E_{\mathrm{fd},d}$ is the latent heat. $T_{\mathrm{f},d}$ can be calculated as:

$$T_{\mathrm{f},d} = \frac{h_{\mathrm{d},d} T_d + h_{\mathrm{c},d} T_{\mathrm{c}} - \dot{m}_d L_d}{h_{\mathrm{d},d} + h_{\mathrm{c},d}}. \tag{20}$$

2.1.5. Interfacial update

To obtain the mass and heat transfer rates in the dth interface, $T_{\mathrm{f},d}$ is required. However, Eq. (20) is non-linear because $Y_{\mathrm{f},d}$ in Eq. (10) is an non-linear (exponential) function of $T_{\mathrm{f},d}$ as in Eq. (13). As a result, the Newton method is adopted to solve for $T_{\mathrm{f},d}$ as follows (OpenFOAM-Foundation, 2020):

$$T_{\mathrm{f},d}^{n+1} = T_{\mathrm{f},d}^{n} - \frac{f(T_{\mathrm{f},d})}{f'(T_{\mathrm{f},d})}, \tag{21}$$

where: $f(T_{\mathrm{f},d}) = h_{\mathrm{d},d}(T_{\mathrm{f},d} - T_d) + h_{\mathrm{c},d}(T_{\mathrm{f},d} - T_{\mathrm{c}}) + \dot{m}_d L_d$, is constructed from Eq. (19), $f'(T_{\mathrm{f},d})$ is its first order derivative, the superscript n represents the known current iteration step, and thus $n+1$ is the unknown next step. The initial guess $T_{\mathrm{f},d}^{1}$ is equal to the converged result of last iteration. After iteration, the converged $T_{\mathrm{f},d}$ will be used in Eq. (10), Eq. (14) and Eq. (15) to update the interfacial mass and heat transfer.

2.2. Population balance equation: the droplet size distribution

The MFM describes droplets of fixed size. To take into account the change of droplet volume caused by condensation or evaporation and predict the evolution of droplet size distribution (DSD), a PBE must be coupled with the MFM. Because of the relatively low volume fraction of the respiratory droplets in the exhaled breath (Chao et al., 2009), their collision, aggregation, and breakup are not considered here. Then, the PBE for a univariate DSD, $n(t, \mathbf{x}, \xi)$, without aggregation and breakup can be written as (Marchisio and Fox, 2013):

$$\frac{\partial n(\xi)}{\partial t} + \nabla \cdot [\mathbf{U}(\xi) n(\xi)] + \frac{\partial}{\partial \xi}[G(\xi) n(\xi)] = 0, \tag{22}$$

where the scalar ξ is the internal coordinate, representing the interested property of the disperse phase, such as size, volume or temperature. The velocity $\mathbf{U}$ is either independent or dependent on ξ. In the first case, droplets of different sizes at a given location move with the same velocity. In the second case, the monokinetic assumption is adopted due to the neglection of interactions between the droplets. Therefore, at a specific location, droplets of the same size will move with the same velocity while those of different sizes can have different velocities. The variable $G = \mathrm{d}\xi/\mathrm{d}t$ is the change rate of the internal coordinate due to condensation and evaporation.

As for the coupling of PBE and MFM, the PBE is used to trace the evolution of the DSD while the MFM is used to describe the motion of the droplets under interactions with the surrounding air flows. Therefore, MFM should provide the velocity $\mathbf{U}$ and the drift rate G for PBE, and PBE should provide DSD to MFM. In MFM, one dispersed phase generally requires only one diameter to calculate the interfacial models at a given location. As a results, the DSD should be converted to one or several representative diameters. In this study, the sectional method (SM) and the quadrature method of moments (QMOM) will be adopted to solve the PBE to trace the dispersion and evaporation of the respiratory droplets. Correspondingly, different DSD conversion methods will be used. The details are presented in the following sections.

2.2.1. Sectional method

The PBE can be solved by using the SM, where the space of the internal coordinate is discretized into a number of intervals, solving the equations for the number density of droplets belonging to each interval. It should be noted that droplets may have all the same velocity or a different velocity for each interval or for groups of intervals. For the former case, Eq. (22) for a volume-based DSD, $n_\mathrm{v}(t, \mathbf{x}, V)$, can be written in the ith interval $I_i = [V_{i-1/2}, V_{i+1/2}]$ as (Lehnigk et al., 2022):

$$\frac{\partial \alpha_\mathrm{d} \rho_\mathrm{d} f_i}{\partial t} + \nabla \cdot (\mathbf{U}_\mathrm{d} \alpha_\mathrm{d} \rho_\mathrm{d} f_i) + V_i \rho_\mathrm{d} (G_\mathrm{v} n_\mathrm{v})\Big|_{V_{i-1/2}}^{V_{i+1/2}} = 0, \tag{23}$$

where $f_i = \alpha_{\mathrm{d},i}/\alpha_\mathrm{d}$ is the size class fraction and $\alpha_{\mathrm{d},i}$ is the volume fraction for the ith size class; $\mathbf{U}_\mathrm{d}$ is the velocity of all droplets and is independent of the internal coordinate V; V_i is the pivotal volume of I_i; $G_\mathrm{v} = \mathrm{d}V/\mathrm{d}t$ is the volume change rate. The third term in the left hand side (LHS) of Eq. (23) is the drift term and can be approximated using an upwind formulation. For evaporation ($G_\mathrm{v} \leq 0$):

$$V_i \rho_\mathrm{d} (G_\mathrm{v} n_\mathrm{v})\Big|_{V_{i-1/2}}^{V_{i+1/2}} = V_i \rho_\mathrm{d} \frac{N_{i+1}}{V_{i+1} - V_i} G_{\mathrm{v},i+1} - V_i \rho_\mathrm{d} \frac{N_i}{V_i - V_{i-1}} G_{\mathrm{v},i}, \tag{24}$$

and for condensation ($G_\mathrm{v} > 0$):

$$V_i \rho_\mathrm{d} (G_\mathrm{v} n_\mathrm{v})\Big|_{V_{i-1/2}}^{V_{i+1/2}} = V_i \rho_\mathrm{d} \frac{N_i}{V_{i+1} - V_i} G_{\mathrm{v},i} - V_i \rho_\mathrm{d} \frac{N_{i-1}}{V_i - V_{i-1}} G_{\mathrm{v},i-1}. \tag{25}$$

In this approach, the coupling between TFM and PBE requires three variables: $\mathbf{U}_\mathrm{d}$, $G_{\mathrm{v},i}$ and d_d. The TFM provides Eq. (23) with $\mathbf{U}_\mathrm{d}$ and $G_{\mathrm{v},i}$ as

$$G_{\mathrm{v},i} = \frac{\dot{m} A_i}{\rho_\mathrm{d} \sum_j N_j A_j}, \tag{26}$$

where $\dot{m}$ is the interfacial mass transfer rate obtained from the TFM and $A_i = 6V_i/d_i$ is the surface area of ith pivotal volume. Additionally, the PBE provides the TFM with the local value of the Sauter mean diameter as:

$$d_\mathrm{d} = \frac{1}{\sum_i \frac{f_i}{d_i}} \tag{27}$$

The Sauter mean diameter is used to represent the DSD and is used as the effective size of the disperse phase to evaluate the drag force and the rates of mass and heat transfer. At each iteration during a time step of the simulation, the PBE is solved first to update d_{d}, with which the TFM is solved to update $\mathbf{U}_{\mathrm{d}}$ and $G_{\mathrm{v},i}$. The iterations stop when a convergence criterion or iteration number is reached.

To model the droplets moving with different velocities, the above method can be extended leading to the multiple size group (MUSIG) method. In MUSIG, each size class or a group of size classes is regarded as a disperse phase, moving with its own velocity. The group velocity can be obtained from the the MFM. More details can be found in Lehnigk et al. (2022). Our MUSIG-based simulations will group the size classes of the PBE into only two disperse phases, small and large droplets, and each moves with its own velocity.

In this study, OpenFOAM v8 (OpenFOAM-Foundation, 2020) is adopted for the sectional method, where the MFM, the evaporation model of section 2.1 and the MUSIG method have been implemented. However, the evaporation model was not combined with the MUSIG method in OpenFOAM v8. Therefore, necessary modifications were made to the code to implement the coupling. The modified solver, denoted as "SM-solver", will be used in the following.

2.2.2. Quadrature method of moments for PBE: single droplet velocity

The PBE can also be solved by the quadrature method of moments (QMOM). In this case, the evolution of integral properties of the DSD, i.e., moments, is evaluated. The diameter-based NDF, $n_{\mathrm{d}}(t, \mathbf{x}, d)$, rather than $n_{\mathrm{v}}(t, \mathbf{x}, V)$ is adopted here to capture accurately the lowest order moments with respect to size and to avoid the too small value of higher order moments. Using QMOM, $n_{\mathrm{d}}(t, \mathbf{x}, d)$ is approximated as:

$$n_{\mathrm{d}}(t, \mathbf{x}, d) \approx \sum_{p=0}^{N-1} w_p(t, \mathbf{x}) \delta(d - d_p(t, \mathbf{x})), \tag{28}$$

where $w_p(t, \mathbf{x})$ and $d_p(t, \mathbf{x})$ are the weight and abscissa of node p, and δ denotes the Dirac delta function. The kth order moment of the NDF can be calculated as:

$$M_k = \int_0^{+\infty} d^k n_{\mathrm{d}}(d) \mathrm{d}d \approx \sum_{p=0}^{N-1} w_p d_p^k. \tag{29}$$

In the simplest case, the moment equations can be derived from Eq. (22) under the assumption that droplets of different sizes share the same velocity field $\mathbf{U}_{\mathrm{d}}$ (i.e., $\mathbf{U} = \mathbf{U}_{\mathrm{d}}(t, \mathbf{x})$ is independent of the internal coordinate d) and can be written as follows:

$$\frac{\partial M_k}{\partial t} + \nabla \cdot (\mathbf{U}_{\mathrm{d}} M_k) + \int_0^{+\infty} d^k \frac{\partial}{\partial d}(G_{\mathrm{d}} n_{\mathrm{d}}) \mathrm{d}d = 0. \tag{30}$$

The third term in the LHS of Eq. (30) is the drift term and is treated following the idea of Yuan et al. (2012), namely, using a time-splitting method to solve the moment equations and modelling the drift term by updating the abscissas. The abscissas are updated as follows:

$$d_p(t + \Delta t) = d_p(t) - G_{\mathrm{d},p} \Delta t, \tag{31}$$

where $G_{\mathrm{d},p}$ is the diameter change rate for pth quadrature node. Additionally, the respiratory droplets generally consist of the volatile water, and the non-volatile biological material, such as virus. In this study, to trace the dispersion of the virus, the virus-laden droplets are not allowed to fully evaporate. After reaching certain minimum size d_{min}, they will stop evaporating and only be transported by the airflow. Therefore, if $d_p(t+\Delta t) < d_{\mathrm{min}}$, then let $d_p(t+\Delta t) = d_{\mathrm{min}}$. This will increase the number of droplets of the minimum size but avoid their further evaporation. Moreover, to be consistent with the evaporation model of section 2.1, the volumetric mass transfer coefficient k_{c} is set as 0 when $d_p(t+\Delta t) \leq d_{\mathrm{min}}$.

To couple the PBE with TFM, similar to the method used in SM, the TFM provides Eq.30 with $\mathbf{U}_{\mathrm{d}}$ and the diameter change rate for pth quadrature node, $G_{\mathrm{d},p}$ as:

$$G_{\mathrm{d},p} = \frac{2}{\rho_{\mathrm{d}} \pi d_p M_1} \dot{m}. \tag{32}$$

And the PBE provides the TFM with the mean disperse phase diameter (Sauter mean diameter) as:

$$d_{\mathrm{d}} = \frac{M_3}{M_2}, \tag{33}$$

similarly, d_{d} representing the DSD is used in the interfacial models.

The detailed algorithm can be found in Appendix A. The solver for this algorithm is developed based on OpenFOAM v2106 (ESI-OpenCFD, 2021) and its module OpenQBMM v7 (Passalacqua et al., 2021), which provides the tools and libraries for multiphase flows and QBMM. This solver can be used to model the droplets moving with the same velocity on varied sizes and it will be denoted as the "mono-solver" in the following sections.

2.2.3. Quadrature method of moments for PBE: size dependent droplet velocity

To model the droplets moving with different velocities on varied sizes, the generalized population balance equation (GPBE) for the diameter-velocity joint NDF, $f_{\mathrm{d}}(t, \mathbf{x}, d, \mathbf{v})$ is generally required, which, however, is relatively complex to solve. In this study, to simplify the problem, the monokinetic assumption is employed:

$$f_{\mathrm{d}}(t, \mathbf{x}, d, \mathbf{v}) = n_{\mathrm{d}}(t, \mathbf{x}, d)\delta\left(\mathbf{v} - \mathbf{U}\left(t, \mathbf{x}, d\right)\right), \tag{34}$$

where $n_{\mathrm{d}}(t, \mathbf{x}, d)$ is the diameter-based NDF and $\mathbf{U}\left(t, \mathbf{x}, d\right)$ is the droplet velocity conditioned on the droplet size d.

The monokinetic assumption is equivalent to assuming that the droplets with the same internal coordinate d move with the same velocity. With this, the GPBE reduces to PBE in Eq. (22) where the velocity $\mathbf{U} = \mathbf{U}\left(t, \mathbf{x}, d\right)$ (Shiea et al., 2020). Similar to section 2.2.2, the transport equation of the kth order size moment M_k can be obtained from Eq. (22) as follows:

$$\frac{\partial M_k}{\partial t} + \nabla \cdot \mathcal{U}_k + \int_0^{+\infty} d^k \frac{\partial}{\partial d}(G_{\mathrm{d}} n_{\mathrm{d}})\mathrm{d}d = 0, \tag{35}$$

where $\mathcal{U}_k = \int_0^{+\infty} d^k n_{\mathrm{d}}(d)\mathbf{U}(d)\mathrm{d}d$ is the kth order velocity moment, which cannot be further simplified as $\mathbf{U}\left(t, \mathbf{x}, d\right)$ depends on the internal coordinate d. To solve for $\mathbf{U}\left(t, \mathbf{x}, d\right)$, the transport equations of velocity moments are introduced following the idea of Heylmun et al. (2019). The equations can be obtained by first multiplying Eq. (22) by $d^k\mathbf{U}(d)$ and then integrating it with respect to the droplet size d:

$$\frac{\partial \mathcal{U}_k}{\partial t} + \nabla \cdot \mathcal{P}_k + \int_0^{+\infty} d^k \frac{\partial}{\partial d}(G_{\mathrm{d}} n_{\mathrm{d}}\mathbf{U})\mathrm{d}d - \int_0^{+\infty} d^k \mathbf{A} n_{\mathrm{d}}\mathrm{d}d = 0, \tag{36}$$

where $\mathcal{P}_k = \int_0^{+\infty} d^k n_{\mathrm{d}}(d)\mathbf{U}(d) \otimes \mathbf{U}(d)\mathrm{d}d$; and $\mathbf{A}\left(t, \mathbf{x}, d\right) = \mathrm{d}\mathbf{U}\left(t, \mathbf{x}, d\right)/\mathrm{d}t$ is the acceleration vector. The relative velocity $\mathbf{V}\left(t, \mathbf{x}, d\right) = \mathbf{U}\left(t, \mathbf{x}, d\right) - \mathbf{U}_{\mathrm{d}}\left(t, \mathbf{x}\right)$ is introduced, where $\mathbf{U}_{\mathrm{d}}\left(t, \mathbf{x}\right)$ is the average velocity of the disperse phase. Then,

$$\mathcal{V}_k = \int_0^{+\infty} d^k n_{\mathrm{d}}(d)\mathbf{V}(d)\mathrm{d}d = \mathcal{U}_k - M_k\mathbf{U}_{\mathrm{d}}. \tag{37}$$

Similarly, $\mathcal{P}_k$ can be divided into two parts: the relative part $\mathcal{P}_{k,\mathrm{r}} = \int_0^{+\infty} d^k n_{\mathrm{d}}(d)\mathbf{V}(d) \otimes \mathbf{U}(d)\mathrm{d}d$, and the average part $\mathcal{P}_{k,\mathrm{a}} = \int_0^{+\infty} d^k n_{\mathrm{d}}(d)\mathbf{U}_{\mathrm{d}} \otimes \mathbf{U}(d)\mathrm{d}d = \mathbf{U}_{\mathrm{d}} \otimes \mathcal{U}_k$. Finally, Eq. (35) and Eq. (36) can be written as:

$$\frac{\partial M_k}{\partial t} + \nabla \cdot \mathcal{V}_k + \nabla \cdot (\mathbf{U}_{\mathrm{d}} M_k) + \int_0^{+\infty} d^k \frac{\partial}{\partial d}(G_{\mathrm{d}} n_{\mathrm{d}})\mathrm{d}d = 0, \tag{38}$$

$$\frac{\partial \mathcal{U}_k}{\partial t} + \nabla \cdot \mathcal{P}_{k,\mathrm{r}} + \nabla \cdot \mathcal{P}_{k,\mathrm{a}} + \int_0^{+\infty} d^k \frac{\partial}{\partial d}(G_{\mathrm{d}} n_{\mathrm{d}}\mathbf{U})\mathrm{d}d - \int_0^{+\infty} d^k \mathbf{A} n_{\mathrm{d}}\mathrm{d}d = 0. \tag{39}$$

When considering N quadrature nodes, there are N unknown weights w_p, N unknown abscissa d_p and $3N$ unknown velocity components. Therefore, $2N$ size moments, namely, M_k where $k = 0, 1, 2, ..., 2N - 1$ are required to obtain w_p and d_p. Additionally, N velocity moment vectors, namely, $\mathcal{U}_k$ where $k = 0, 1, 2, ..., N - 1$ are required to obtain the pth quadrature node velocity $\mathbf{U}_p = (U_{x,p}, U_{y,p}, U_{z,p})$. The transport equations of size moment and velocity moment, as in Eq. (38) and Eq. (39), are solved by using a time-splitting method, where the drift term for the droplet size and the velocity acceleration term are modelled by updating the diameter and velocity abscissas as in section 2.2.2 and in Heylmun et al. (2019), respectively.

For the coupling of PBE and TFM, the droplets are moving with different velocities, therefore, the interfacial models should consider the interactions with each quadrature node. Take the drag force for example, in this case, the drag force in the momentum equations is written as:

$$\mathbf{F}_{\mathrm{D,d}} = \sum_{p=0}^{N-1} \mathbf{F}_{\mathrm{D,d},p} = \sum_{p=0}^{N-1} \left(\frac{3}{4} C_{\mathrm{D},p} \mathrm{Re}_p \frac{\alpha_{\mathrm{d},p} \rho_{\mathrm{c}} \nu_{\mathrm{c}}}{d_p^2} (\mathbf{U}_{\mathrm{c}} - \mathbf{U}_p) \right), \tag{40}$$

where $\mathbf{F}_{\mathrm{D,d},p}$ is the drag force acted on the pth node, $C_{\mathrm{D},p}$ and Re_p are the drag coefficient and Reynolds number calculated using the pth node velocity $\mathbf{U}_p$, $\alpha_{\mathrm{d},p} = (\alpha_{\mathrm{d}} w_p d_p^3)/M_3$ is the volume fraction of the pth node. Other interfacial models are calculated in a similar way, replacing the velocities, volume fractions and diameters with those of the pth node and making a summation. Therefore, the PBE should provide the TFM with $\alpha_{\mathrm{d},p}$, d_p and $\mathbf{U}_p$ for the calculation of interfacial models, while the TFM should provide PBE with $\mathbf{U}_{\mathrm{d}}$ for the relative velocity and the interfacial mass transfer rate of the pth node $\dot{m}_p$ for $G_{\mathrm{d},p}$ as:

$$G_{\mathrm{d},p} = \frac{2}{\rho_{\mathrm{d}} \pi w_p d_p^2} \dot{m}_p. \tag{41}$$

The detailed algorithm can be found in Appendix B. The solver for this algorithm is developed based on the tools and libraries of OpenFOAM v2106 and OpenQBMM v7. This solver can be used to model the droplets moving with the different velocities on varied sizes and will be denoted as "poly-solver" in the following sections.

3. Verification and Validation

As previously mentioned, polydispersity and evaporation are important features of respiratory droplets and can significantly affect their space and time evolution. Therefore, the ability of the developed CFD-PBE approach to deal with these features are assessed carefully in this section, by using the test cases of increasing complexity. The evaporation model is validated first using the reported temporal evolution of the diameter of a single droplet (section 3.1) and freely falling droplets (section 3.2). Then, the reliability of the CFD-PBE approach to simulate the non-evaporating particle flows are evaluated by using two test cases: one concerning the evolution of the exhaled breath of respiratory activities (section 3.3) and the other concerning the flow field and the particle dispersion in a chamber (section 3.4). Finally, the CFD-PBE approach is applied in the transport of evaporating cough droplets in a 3D chamber and compared with numerical results in the literature (section 3.5).

3.1. Verification of the evaporation model

The evaporation model is of great importance because it provides the interphase mass transfer rate, not only for the TFM but also for the PBE. Therefore, it is verified first against the experimental result of droplet size variations with time of an evaporating pure water droplet from Lieber et al. (2021). In their experiment, a single droplet was injected into the process chamber, levitated in the air by an acoustic levitator and evaporating at constant temperature and relative humidity (RH). The evaporation process of the droplet was recorded by using microscopic imaging. Additionally, special attention was paid to minimize the influence of the experimental setup, such as using high resonance frequency of 100kHz to reduce the effect of acoustic streaming.

To verify the evaporation model of the TFM, it can be rewritten for a single stationary evaporation droplet in the following form:

$$\frac{\mathrm{d}m_{\mathrm{d}}}{\mathrm{d}t} = \dot{m}_{\mathrm{d}} = \rho_{\mathrm{c}} k_{\mathrm{d}} (Y_{\mathrm{f}} - Y_{\mathrm{H_2O}}), \tag{42}$$

$$\frac{\mathrm{d}m_{\mathrm{d}} E_{\mathrm{d}}}{\mathrm{d}t} = Q_{\mathrm{fd}} - \dot{m}_{\mathrm{d}} E_{\mathrm{fd}} = h_{\mathrm{d}} (T_{\mathrm{f}} - T_{\mathrm{d}}) - \dot{m}_{\mathrm{d}} E_{\mathrm{fd}}, \tag{43}$$

where m_d is the mass of the droplet, E_d is the internal energy of the droplet, $k_\mathrm{d} = \pi d_\mathrm{d}\mathrm{Sh}D_\mathrm{c}$, is the mass transfer coefficient of the droplet, $h_\mathrm{d} = 10\pi d_\mathrm{d}\kappa_\mathrm{c}$, is the heat transfer coefficient within the droplet and, $h_\mathrm{d} = \pi d_\mathrm{d}\mathrm{Nu}\kappa_\mathrm{c}$, is the heat transfer coefficient of the droplet to its surrounding. The simplified evaporation model is a system of two ordinary differential equations (ODEs). This is solved by using a developed python code, where T_f is iteratively solved first as in section 2.1.5, and then Eq. (42) and Eq. (43) are solved.

For the verification, an ambient temperature (T_g) of 296.15 K and a relative humidity of 50% are adopted and kept constant during the simulation, as in Lieber et al. (2021). The initial temperature of the droplet (T_d) is also 296.15 K and the initial diameter (d_0) is 215 μm. The thermal properties of the droplet and the surrounding air can be found in Appendix C. Figure 1 shows the temporal evolution of the normalized surface of the water droplet. It can be seen that the predicted result is in good agreement with the experiments. An approximately linear evolution of the normalized surface d^2/d_0^2, known as the classical d^2-law (Dalla Barba et al., 2021), is observed. This is because when the forced and natural convection is small, the surface of an evaporating droplet decreases linearly at a rate depending on ambient properties (Faeth, 1979). Therefore, we can conclude that the evaporation model and the thermal physical property models are verified.

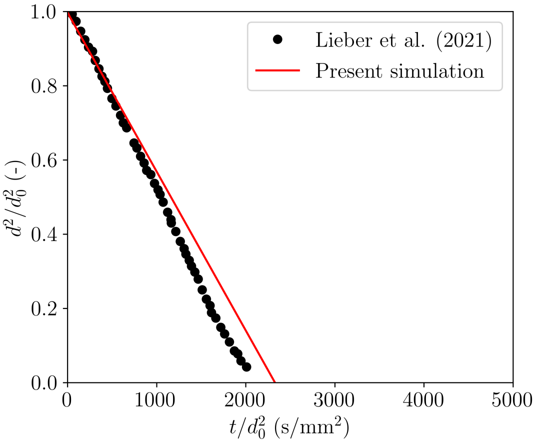

Figure 1: Temporal evolution of the normalized surface of a water droplet.

3.2. Validation of the evaporation model of the PBE

After the verification of the evaporation model, the ability of PBE to trace the droplet size changes of evaporating droplets within the frame of the TFM is assessed. The two PBE solving methods, SM and QMOM, are validated with the diameter changes of evaporating droplets reported by Redrow et al. (2011) and Wei and Li (2015), which are widely used in the validation of the evaporation model (Li et al. (2018), Yan et al. (2019), Li et al. (2020), Sen (2021), Mirikar et al. (2021) and Yan et al. (2022)). To reproduce the results reported in literature, the setups of Li et al. (2018) are adopted, where the droplets are freely falling and evaporating in quiescent air.

As shown in Figure 2, a two-dimensional (2D) chamber (4 m length × 3 m height) is adopted as geometry. The droplets are initially located in the red square region, whose size is 0.2 m × 0.2 m and center is at $x = 2$ m and $z = 2$ m. The droplets are released with zero initial velocity. To match the E-L approach used in the reference paper, a very low initial volume fraction for the droplets, $\alpha_\mathrm{d} = 1 \times 10^{-6}$, is specified. The evaporation of droplets of two sizes, 10 μm and 100 μm, under two relative humidities of 0% and 60%, are simulated respectively. The droplet temperature T_d is 310.15 K and the environment temperature T_c is 298.15 K as in Redrow et al. (2011).

For the simulation, the SM-solver and the QMOM mono-solver are used and compared. A uniform grid with 30000 square cells (200 × 150) is adopted here. Both phases are considered as laminar due to their low velocities. The thermal physical property models are set as in Appendix C. For the SM-solver, 21 pivotal volumes are specified to divide the interval from the initial droplet size to the minimum size. For the QMOM mono-solver, two nodes are used and four moments equations are thus solved. The initial values for the moments are reported in Table 1.

The predicted droplet size changes by using the SM and the QMOM are compared with literature data as shown in Figure 3. The numerical results of both methods agree well with the literature data. The effects of initial size and relative humidity are also presented as: smaller droplets (10 μm) evaporate faster than larger droplets (100 μm); increasing the relative humidity will reduce the evaporation rate. Therefore, the CFD-PBE approach can trace the diameter changes of evaporating droplets under different conditions.

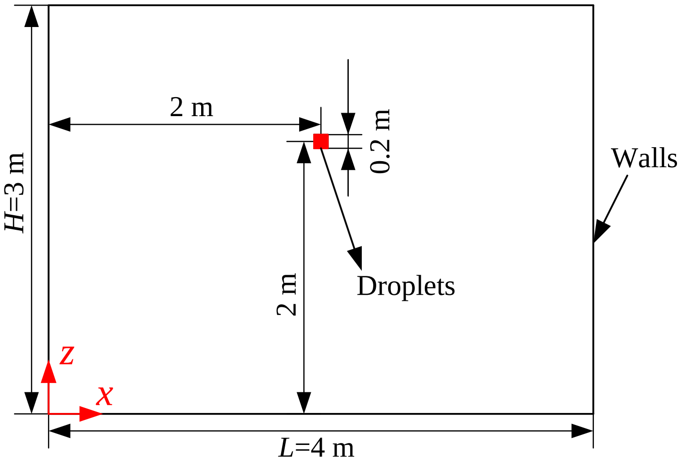

Figure 2: Geometry of 2D chamber.

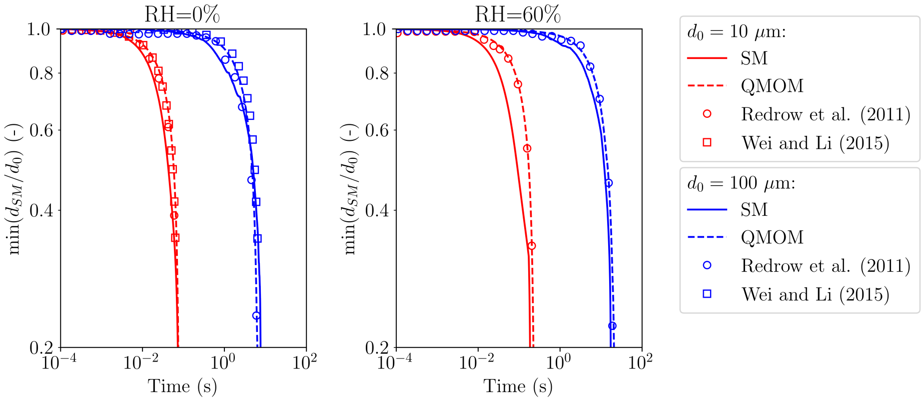

Figure 3: Droplet size time evolution by using SM and QMOM.

Table 1
Initial volume fraction and moments for the droplets of the two sizes.

Diameter (μm)	α_d (-)	M_0 (m^{-3})	M_1 (m^{-2})	M_2 (m^{-1})	M_3 (-)
10	1×10^{-6}	1.909859×10^{9}	1.909859×10^{4}	1.909859×10^{-1}	1.909859×10^{-6}
100	1×10^{-6}	1.909859×10^{6}	1.909859×10^{2}	1.909859×10^{-2}	1.909859×10^{-6}

3.3. Droplet transport in exhaled breath

The respiratory droplets are carried by and interact with the expelled airflow. Therefore, an accurate description of the respiratory airflow is essential for the prediction of the dispersion and evaporation of the droplets. To assess the reliability of the CFD-PBE approach in the simulations of respiratory activities, the QMOM mono-solver and the QMOM poly-solver (i.e., the solver considering the effect of size on droplet velocity) are validated against the experimental data from Wang et al. (2021a), where the distance traveled by the front of a sneeze jet was measured.

In their experiment, the jet was expelled from the mouth, a circular opening, of a dummy head to mimic a sneeze. The diameter of the mouth was 2 cm. A gamma function was adopted as the time-varying inlet velocity for a sneeze lasting for 0.6 second. The jet was seeded with non-evaporating droplets ($\rho_\mathrm{d} = 1000\,\mathrm{kg\cdot m^{-3}}$) and a high-speed camera was used to visualize the flow field and track the jet front. The sizes of the droplets ranged from 1-3 μm, having an average size of 2 μm. The volume fraction of the droplets was set to 4.55×10^{-6}. The temperature of the environment, jet and droplets are identical and constant, equal to 295 K. And the relative humidities of the environment and jet are also identical and constant, equal to 50%.

For the simulation, the geometry of the 3D chamber discussed in detail in section 3.5 is adopted. Both the mono-solver and the poly-solver are used to solve the TFM and PBE to trace the evolution of sneeze jet front with advancing time. The RNG $k - \epsilon$ model is used for the continuous phase while the laminar flow assumption is used for the disperse phase. During the simulation, the evaporation model is disabled to mimic the experiment. The thermal physical properties in Appendix C are used. The boundary conditions and initial fields are given as in the experiment, namely, specifying a time-varying velocity condition at the inlet, open to air at the right boundary and no-slip conditions at other boundaries. For the setup of QMOM, two nodes are adopted, so four moment equations are solved. At the inlet, the moments of the DSD are calculated by using the volume fraction and the DSD from the experiment (see Table 2).

The travelling distance of the sneeze jet front L is extracted through setting a threshold for the disperse phase volume fraction, α_d, and by selecting the maximum distance from the mouth where the breathe is released at each time step. The threshold value is prescribed as $\alpha_\mathrm{d} = 1 \times 10^{-10}$. Particles are regarded as actually existing in the cells where $\alpha_\mathrm{d} \geq 1 \times 10^{-10}$, and the maximum x-coordinate of those cells is the travelling distance at each time step.

Table 2
Moments at the inlet for the case of sneeze jet front.

α_d (-)	M_0 (m^{-3})	M_1 (m^{-2})	M_2 (m^{-1})	M_3 (-)
4.55×10^{-6}	1.277276×10^{12}	2.360087×10^{6}	4.472296	8.689860×10^{-6}

The predicted and measured temporal evolution of the sneeze jet front are shown in Figure 4. It can be seen that the numerical results of both solvers are very close and are in good agreement with the experimental result. This indicates that the poly-solver is reliable for the flows where the droplet size distributes in a narrow range, such as in droplet nuclei dispersion. In addition, the evolution of exhaled breath can be divided into two stages: the jet stage and the puff stage. In the early jet stage, the sneeze continues, constantly providing momentum to the exhaled jet and resulting in the self-similar behavior of $L \propto t^{1/2}$. In the late puff stage, the sneeze stops, leading to the constant momentum of the exhaled jet and the self-similar behavior of $L \propto t^{1/4}$. The different behaviors of jet and puff stage are expected to affect the droplets dispersion and evaporation (Rosti et al., 2021), making it important to capture such features. It can be seen that the two scaling laws and their transition are accurately captured by both numerical and experimental results. Therefore, the developed mono-solver and poly-solver for the CFD-PBE approach are validated against the experimental data of a respiratory activity, a sneeze, and are capable of accurately predicting the two-stage evolution of the exhaled breath.

3.4. Validation for the aerosols transmission

The previous analysis confirms the ability of the QMOM poly-solver to describe droplet transport during respiratory activities. However, in a closed environment, such as a chamber, the behavior of the dispersion changes because of the role played by other phenomena, such as droplet settling, flow confinement or recirculation. Therefore, the reliability of the CFD-PBE approach to predict the space and time evolution of the aerosols in a three-dimensional (3D) chambers is also assessed by comparing its results with the experimental data of Chen et al. (2006). In their experiment, non-evaporating particles (10 μm) and airflow are injected into a 3D chamber from the inlet on the left side and leave the chamber from the outlet on the right side. The gas phase velocity profiles and the normalized concentration at specific locations in the center plane were measured.

The geometry is shown in Figure 5. The size of the chamber is: length × width × height = 0.8 m × 0.4 m × 0.4 m. To match the experimental setups, the inlet and outlet are extended 0.2 m out of the chamber. They are of the same size, 0.04 m × 0.04 m, and their centers are located at $x = -0.2$ m, $y = 0$ m, $z = 0.36$ m and $x = 1.00$ m, $y = 0$ m, $z = 0.04$ m, respectively. Only half of the 3D chamber is selected as computing domain due to symmetry. A multi-block structured grid with 67520 cube cells is adopted in this study. The grids of similar scale have been proved

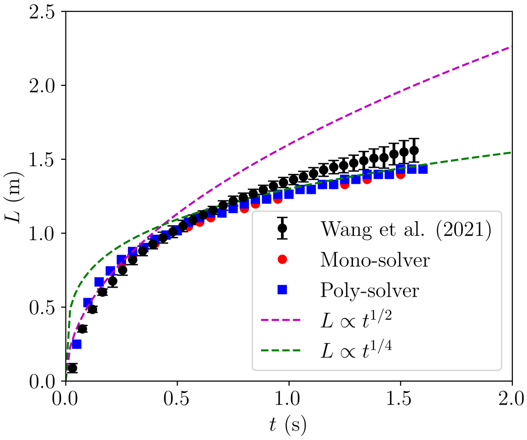

Figure 4: Temporal evolution of the sneeze jet front.

to be reliable in Chen et al. (2006) and Huang et al. (2022). For boundary conditions, the inlet velocity is 0.225 $\mathrm{m \cdot s^{-1}}$. The disperse phase volume fraction at the inlet is $\alpha_\mathrm{d} = 5 \times 10^{-8}$, to match the experiment. The system is isothermal at 293.15 K. The boundaries except the symmetric plane and inlet/outlet regions, are set as no-slip walls. The particle density is 1400 $\mathrm{kg \cdot m^{-3}}$ as in experiment.

The QMOM poly-solver is adopted again to solve the TFM and PBE to trace the particles. The setup is similar to Section 3.3: the RNG $k - \epsilon$ model for the continuous phase and laminar for the disperse phase, disabled evaporation model, and two nodes for the QMOM. The moments at the inlet are also evaluated using α_d and droplet size distribution (8 μm to 13 μm) of the experiment and are listed in Table 3.

The transient simulation is performed for a time long enough to reach the steady state as in the experiment. Then, the profile of x direction continuous phase velocity (U_x) and the disperse phase volume fraction α_d at x =0.2 m, 0.4 m and 0.6 m in the center plane are extracted. The normalized concentration is calculated as $\bar{C} = \alpha_\mathrm{d}/\alpha_\mathrm{d,inlet}$. The comparison of predicted and measured U_x and $\bar{C}$ are shown in Figure 6. Because of the inlet jet flow, both U_x and $\bar{C}$ are high in the upper region of the chamber ($z = 0.2$ m to $z = 0.4$ m). The jet also causes air recirculation in the chamber. Therefore, a relatively uniform negative U_x is found in the bottom region ($z = 0$ m to $z = 0.2$ m), and the aerosols, carried by the air recirculation, are uniformly dispersed here. As the jet advances from $x = 0.2$ m to $x = 0.6$ m, U_x and $\bar{C}$ decrease and diffuse to surrounding regions, showing a typical jet evolution. Additionally, it should be noted that $\bar{C}$ is extremely high on the lower wall, indicating that the particles are accumulating there. This is caused by the boundary conditions: the no-slip boundary condition for continuous and disperse phase velocity and the zero gradient boundary condition for volume fractions and moments. The particles cannot leave the computing domain and thus accumulate there. Although this effect could be removed by specifying a particle depositing boundary condition as in Chen et al. (2006), we did not implemented it because the inaccuracy is restricted to a very thin layer close to the lower wall and does not affect the remaining portion of the profile. The predicted results agree well with the measured results indicating that the CFD-PBE approach can be used to trace both flow and concentration fields of aerosols in the 3D chamber and the developed codes are reliable.

Table 3
Moments at the inlet for the case of aerosols transmission.

α_d (-)	M_0 ($\mathrm{m^{-3}}$)	M_1 ($\mathrm{m^{-2}}$)	M_2 ($\mathrm{m^{-1}}$)	M_3 (-)
5×10^{-8}	9.587645×10^{7}	9.561545×10^{2}	9.548915×10^{-3}	9.549295×10^{-8}

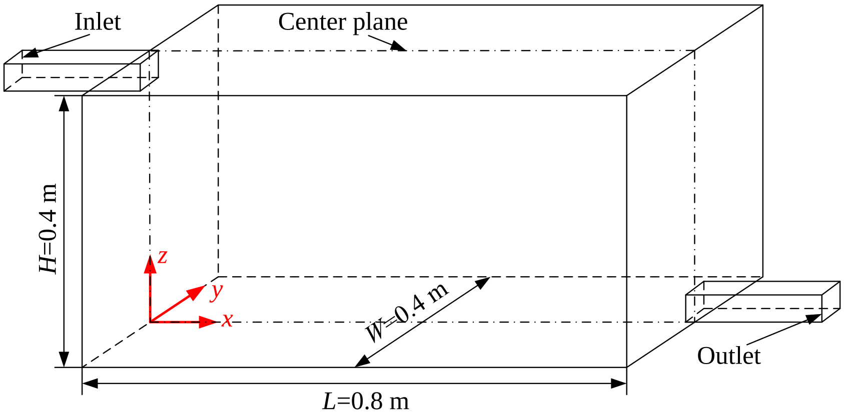

Figure 5: Geometry of a ventilated 3D chamber model.

3.5. Cough droplets in 3D chamber

3.5.1. Geometry and numerical setups

Eventually, the CFD-PBE approach is applied in the dispersion and evaporation of cough droplets in a 3D chamber and compared with the numerical results using E-L approach reported by Li et al. (2018). The geometry identical to that in Li et al. (2018) is shown in Figure 7, the size of which is length × width × height = 4.0 m × 2.0 m × 3.0 m. The mouth (inlet) is modelled by a circle, whose diameter is 2 cm. Its center is located at $x = 0$ m, $y = 0$ m, $z = 2.0$ m. The right boundary (or outlet) is open to atmosphere. The bottom wall is also set as outlet. This is to avoid the accumulation of the droplets in the near-wall cells, which might affect the stability of the poly-solver. Additionally, only half of the chamber is built as computing domain in order to reproduce the settings used by Li et al. (2018). Therefore, the front boundary is set as symmetric plane. All other boundaries are no-slip walls.

The multi-block structured grid is built for the computing domain. The grid is refined in the near-wall regions and the inlet region. The grid convergence is examined using three grids having 364640 (coarse), 831220 (middle) and 1912700 (fine) cube cells, respectively. It is found that the middle grid of 831220 cells shows good consistency with the fine grid and thus is adopted in this study. The details can be found in Appendix D

To compare with Li et al. (2018), the same boundary conditions are used in this study. The ambient temperature is 298.15 K and relative humidity is 50%. The cough jet temperature is 310.15 K and relative humidity is 100%. The temperature of cough droplets is also 310.15 K. To mimic a single cough, a time varying inlet velocity obtained from the experiment of Gupta et al. (2009) is specified for the continuous phase. The cough lasts for 0.5 s with the maximum velocity of 13.4 $\mathrm{m \cdot s^{-1}}$ at 0.08 s, as shown in the left figure of Figure 8a. The droplets are injected into the chamber with the same instantaneous velocity as the continuous phase. The droplet size distribution obtained from the experimental data of Chao et al. (2009) is given at the inlet. As shown in the right figure of Figure 8b, the droplet sizes range from 3 μm to 750 μm, and it can be noted that a huge number of small droplets only have a very low volume fraction while the large droplets are contrary. The disperse phase volume fraction α_d at the inlet is 2.323×10^{-4}, which is equivalent to a total injected amount of 100 mg.

For the transient simulation of the cough droplets, the SM-solver and the QMOM poly-solver are adopted to trace the droplets moving with different velocities on the various sizes. The RNG $k-\epsilon$ model is used for the continuous phase while laminar for the disperse phase. The thermal physical property models in Appendix C are adopted. A minimum diameter of 1 μm is specified for the evaporation model. After evaporation into the minimum diameter, the droplets will stop further evaporation, and they will only be dispersed by the airflow, leading to an accumulation of droplets in an indoor environment.

For the SM-solver, 17 pivotal volumes are used to cover the experimental DSD of Chao et al. (2009). To model the multiple velocities of the droplets, a two-class MUSIG is adopted. As mentioned before, 100 μm is the crucial size (Mittal et al., 2020), which differentiates the behavior of the droplets of different sizes. Therefore, the droplets are divided into two disperse phases as shown in Table 4, where the pivotal volumes are converted into pivotal diameter for clarity. The first disperse phase contains the small droplets (<100 μm), including 10 pivotal volumes (from No. 1 to 10), whose volume fraction at the inlet is 5.7×10^{-7}. The second one contains the large droplets (>100 μm), including

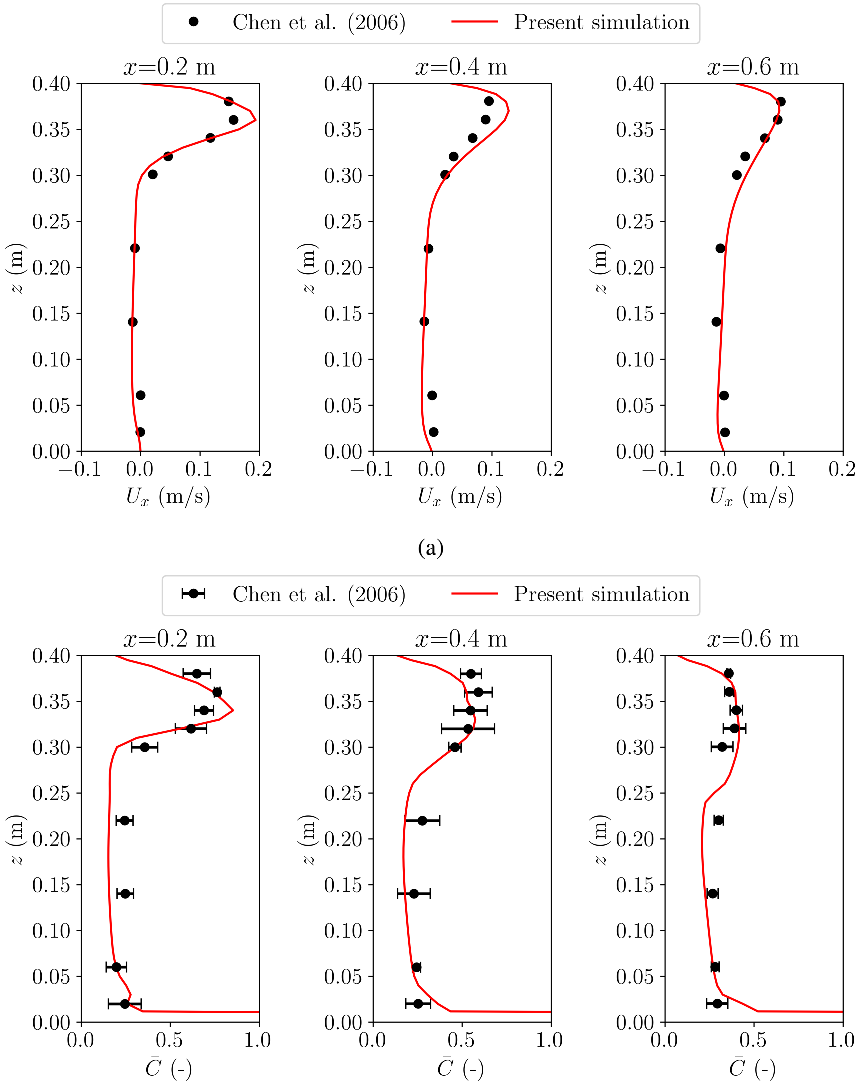

(a)

(b)

Figure 6: The comparison of predicted and measured profiles at x = 0.2, 0.4 and 0.6 m in the center plane: (a) the x direction continuous phase velocity U_x, (b) the normalized concentration $\bar{C}$.

7 pivotal volumes (from No. 11 to 17), whose volume fraction at the inlet is 2.3173×10^{-4}. The velocities of the two disperse phases can be obtained by solving the three-fluid E-E model.

For the QMOM poly-solver, two nodes are adopted to trace the behavior of droplets. The moments are calculated by using the DSD in Figure 8b and scaled to match α_d at the inlet. The details are reported in Table 5. At the inlet, the two abscissas or node diameters are 21.6 μm and 550.7 μm, respectively. One is indeed smaller than 100 μm while the other is larger than 100 μm. Therefore, both small and large droplets can be represented by the quadrature nodes.

3.5.2. Results and discussion

Figure 9 and Figure 10 show the results obtained by using the SM. Figure 9a shows the predicted volume fraction of the disperse phase for small droplets $\alpha_\mathrm{d,S}$. The small droplets mainly suspend in the air and travel a relatively short distance. This is because the small droplets, owning small momentum response time (or inertia), tend to be carried by the airflow. In addition, it can be noted that even the small droplets show a falling trend especially at t=0.5 s. A check of the volume fraction of the different size classes belonging to small droplets, reported in Figure 10a, shows

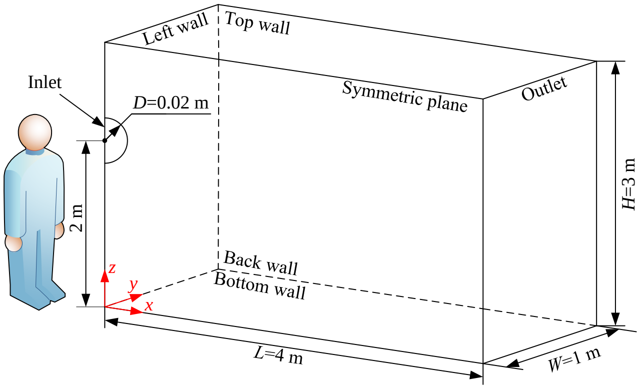

Figure 7: Geometry of 3D chamber.

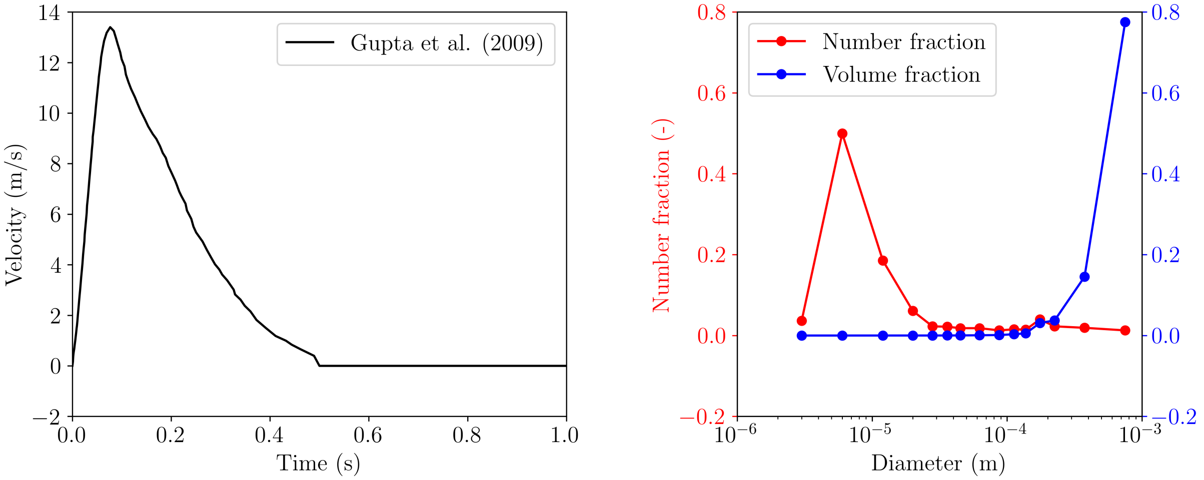

(a)

(b)

Figure 8: The cough jet and droplets inlet boundary conditions: (a) the velocity of a single cough (Gupta et al., 2009), (b) the number and volume fraction of the cough droplets (Chao et al., 2009).

that the falling trends is mainly caused by 10th and 9th size classes, which represent the size of 87.5 μm and 62.5 μm, respectively. For smaller size classes, the falling trends disappear and only a suspending trend is observed for the 5th size class (20 μm) in Figure 10a. This indicates that the size of 100 μm might be a little large to differentiate the small and large droplets.

The volume fraction of the disperse phase for large droplets $\alpha_{\mathrm{d,L}}$ is shown in Figure 9b. The large droplets show a remarkable falling trend and no suspending trends are observed because of gravity. By inspecting the volume fraction of different size classes belonging to large droplets (Figure 10b), it can be seen that the droplets of all the size classes belonging to the large droplets are falling. This again implies that the crucial size of 100 μm is large enough. Additionally, before settling, say at t=0.1, 0.3 or 0.5 s, the large droplets travel longer distance than small droplets. This is because the large droplets have larger momentum response time (or inertia), less affected by the originally still indoor air, travelling a longer distance with their high initial velocity. However, after the settlement of the large droplets, the small droplets keep suspending in the air and can be transported for longer distance. In particular, affected by the time-varying inlet velocity and gravity, the large droplets cloud show a leftward-opening parabola shaped distribution. The droplets released at the beginning and the ending of the cough might have the same x-coordinate (horizontal distance) but different z-coordinates (height). The similar pattern was also found in Dbouk and Drikakis (2020), where the E-L approach was used for the cough droplets.

Table 4
Size groups of the disperse phase for small and large droplets.

Small droplets (< 100 μm)			Large droplets (> 100 μm)		
No.	d (μm)	f_i (-)	No.	d (μm)	f_i (-)
1	1.0	0	11	112.5	3.18×10^{-3}
2	3.0	5.76×10^{-5}	12	137.5	5.47×10^{-3}
3	6.0	6.33×10^{-3}	13	175.0	3.10×10^{-2}
4	12.0	1.88×10^{-2}	14	225.0	3.75×10^{-2}
5	20.0	2.86×10^{-2}	15	375.0	1.46×10^{-1}
6	28.0	2.93×10^{-2}	16	750.0	7.77×10^{-1}
7	36.0	5.97×10^{-2}	17	1500.0	0
8	45.0	9.71×10^{-2}			
9	62.5	2.60×10^{-1}			
10	87.5	5.00×10^{-1}			

Table 5
Moments at the inlet for the case of cough droplets.

α_d (-)	M_0 (m^{-3})	M_1 (m^{-2})	M_2 (m^{-1})	M_3 (-)
2.323×10^{-4}	6.411369×10^{7}	2.792789×10^{3}	8.334057×10^{-1}	4.436603×10^{-4}

The Sauter mean size for the two disperse phases are shown in Figure 9c. The size change due to evaporation is not significant. The initial Sauter mean size for small and large droplets phase are 53.2 μm and 544.5 μm, respectively. According to the d^2-law in section 3.2, even for the small droplets, the time required for full evaporation is in order of several seconds. Therefore, at t=0.5 s, both droplets have not evaporated remarkably.

The Figures 11 to 13 show the results obtained by using the QMOM. Figure 11 gives the evolution of the disperse phase volume fraction, α_d. Similar to the results obtained with the SM-solver and in Li et al. (2018), the suspension of small droplets and the falling of large droplets are observed. It should be noted that the quadrature nodes in QMOM represent the dynamic size distribution rather than the fixed size classification in the SM. Therefore, the conclusion cannot be drawn only from Figure 11, but also with the help of the quadrature node distribution in Figure 12. As mentioned before, the inlet quadrature nodes are 21.6 μm and 550.7 μm, respectively. Since they can move with different velocities, the small droplets initially represented by the 1st node will evaporate remarkably, suspend in the air and form a suspending droplets cloud while the large droplets initially represented by the 2nd node will evaporate slightly, fall in the air and form a falling droplets cloud. Therefore, the size distribution moves toward smaller sizes in the suspending cloud and moves towards larger sizes in the falling cloud. The changing DSD results in the changes of the quadrature nodes. Finally, the decreasing 2nd node diameters in Figure 12b together with the small 1st node diameter represent the small droplets that are found to be suspending. Meanwhile, the increasing 1st node diameters in Figure 12a together with the large 2nd node diameter represent the large droplets that are found to be falling.

Figure 13 shows the 0th order moment M_0, representing the droplets number density. Again, the suspending or falling trends are found. Comparing Figure 11 with Figure 13, it can be found that the suspending small droplets have a huge number density but a small volume fraction. For other respiratory activities, like speaking, less droplets are expelled. After evaporation, the volume fraction for the small droplets might be extremely small, which might result in the difficulty in analysis.

Furthermore, the parabola-like pattern of the large droplets cloud in Dbouk and Drikakis (2020) is also observed in Figure 13 though not as remarkable as in SM. This is because the diameter of large droplets in SM is smaller than that in QMOM. So, the large droplets in QMOM have larger mass or inertia and thus they are less affected by the originally still indoor air. Finally, they are not exceeded too much by the later released droplets, resulting in less remarkable parabola-like pattern. The droplets trajectories at 0.5 s and 2.0 s are compared with those in Li et al. (2018), where the maximum droplet travelling distance at 0.5 s and 2.0 s are approximately 2.70 m and 3.25 m, respectively. In this study, the travelling distances are 2.95 m at 0.5 s and 3.20 m at 2.0 s. Good agreement is observed. And identical to

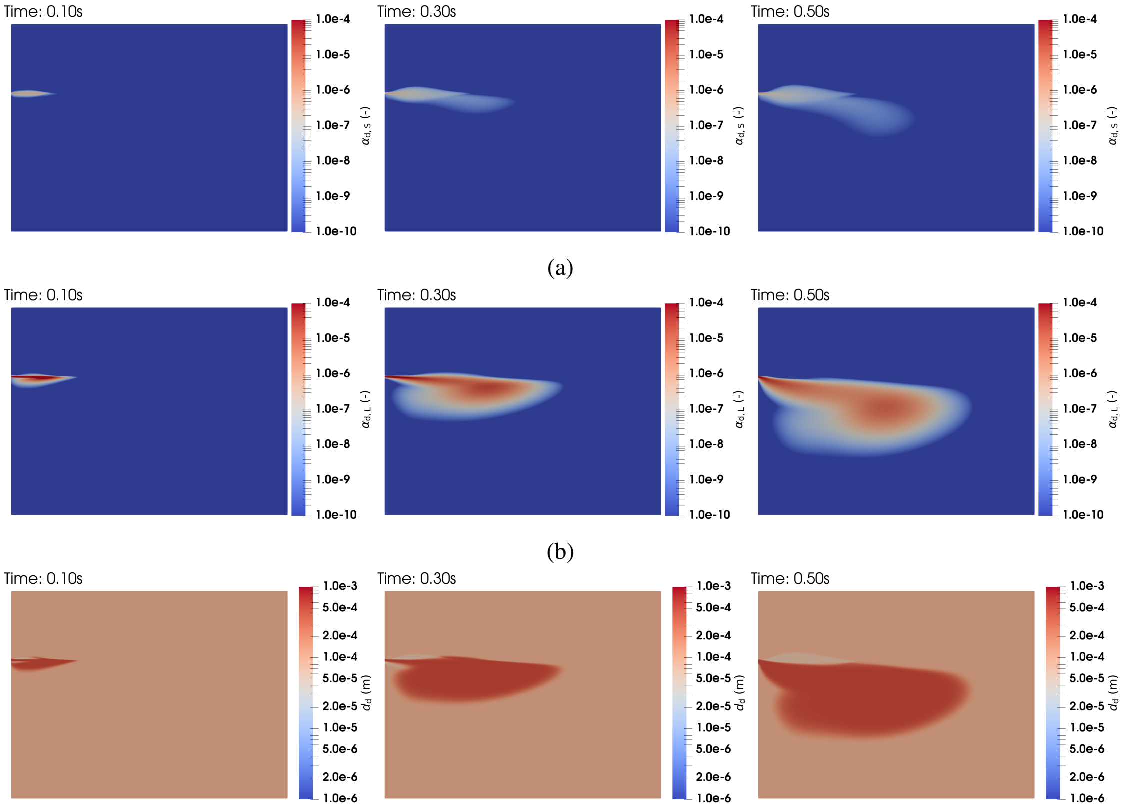

(a)

(b)

(c)

Figure 9: The variables of the disperse phase obtained by using the SM-solver in the symmetry plane at different times, from left to right: t=0.1, 0.3 and 0.5 s: (a) volume fraction for small droplets $\alpha_{d,S}$, (b) volume fraction for large droplets $\alpha_{d,L}$, (c) mean disperse phase diameter d_d.

the conclusion of Li et al. (2018): large droplets settle on the ground within 2.0 s. Therefore, the results obtained by using the CFD-PBE approach can be regarded as reliable.

The disperse phase volume fraction α_d and diameter d_d obtained by using SM and QMOM are compared in Figure 14. As shown in Figure 14a, the vertical distribution of the droplets, represented by α_d and predicted by the two approaches, is similar. The cough jet is injected at the height of z = 2.0 m. Because of the gravity, the most part of the droplet jet falls. Therefore, the main peak of the α_d distribution is below z = 2.0 m. Additionally, both SM and QMOM show an additional peak above the main jet, while SM also shows an additional peak below the main jet. The former is caused by the suspension of the small droplets. As mentioned before, the suspending trend is more significant in QMOM due to its lower initial 1st node diameter and thus its peak is more significant. The latter is caused by the parabola-like pattern, which is more remarkable in SM than in QMOM. Therefore, such a peak is not captured by QMOM. Figure 14b shows the distribution of d_d along horizontal lines at different heights. Similarly, in regions where droplets actually exist, d_d above the inlet (z = 2.0 m) is small and changes remarkably while that below the inlet is large and almost keep constant. Furthermore, it can be noted that in regions having no droplets, for example, z = 1.8 m and x = 3 to 4 m, d_d obtained by SM and QMOM are different. This is caused by the different methods to calculate the dispersed phase diameter with absence of droplets. Since there are no droplets, this will not affect the main flow. This d_d distribution, again, shows the different behaviors of small and large droplets under gravity and evaporation.

Finally, the advantages and disadvantages of SM and QMOM are discussed here. The simulations are parallelized on a workstation with an Intel Xeon CPU E5-2630 v4 (2.20GHz, 10 cores). The average time (averaged on first 5000 time steps) for every 1000 time steps of SM and QMOM are 4.8 hours and 6.32 hours, respectively. SM has relatively lower costs than those of QMOM in the case and setup of this study. This is because, QMOM has more equations to solve, and QMOM also has additional costs of moments inversion. However, it should be noted that two nodes are used

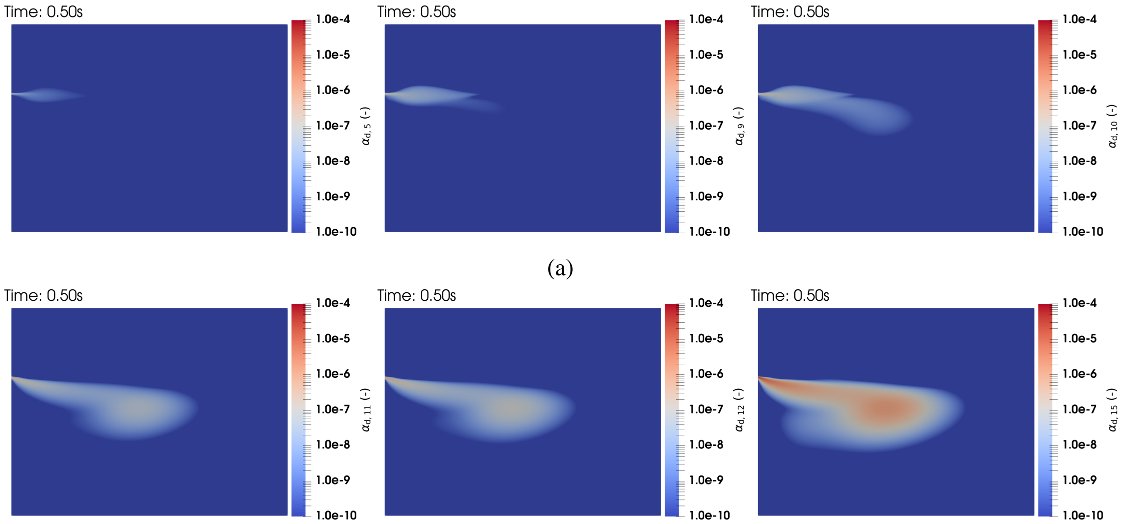

(a)

(b)

Figure 10: The volume fraction of the size classes obtained using SM-solver in the symmetry plane at t=0.5 s: (a) for small droplets: 20 μm ($\alpha_{\mathrm{d},5}$), 62.5 μm ($\alpha_{\mathrm{d},9}$) and 87.5 μm ($\alpha_{\mathrm{d},10}$), (b) for large droplets: 112.5 μm ($\alpha_{\mathrm{d},11}$), 137.5 μm ($\alpha_{\mathrm{d},12}$) and 375 μm ($\alpha_{\mathrm{d},15}$).

in the QMOM simulation of this study. The first four moments are solved and traced, including M_2, the total surface area of droplets, which is of great importance in droplets evaporation according to the d^2 law. As for SM, only the total number and total volume are traced (equivalently, M_0 and M_3 in QMOM). The results of SM in this study are acceptable and in good agreement with literature, but in other cases, more size classes might be required by SM to make up for the missing of total surface area. Obviously, this would increase the computational costs of SM.

Additionally, to model the different velocities of droplets with different sizes, the SM (MUSIG method) requires to manually divide the size classes into several groups and define each of them as a disperse phase to obtain their different velocities. Inappropriate criteria can result in unreasonable results, such as the group of small droplets showing a falling trend. On the contrary, the QMOM uses the quadrature nodes obtained from quadrature method to represent the droplets moving with different velocities. No explicit interaction is required, which can provide a better representation of the behavior of the polydisperse droplets.

As for the post-processing, both methods can directly provide variables, like the droplets volume fraction, for analyses. Furthermore, QMOM can directly provide the number density M_0, which is especially helpful in the simulations having a too low volume fraction to analyze.

4. Conclusions

The knowledge of the dispersion and evaporation of the respiratory droplets is of great importance to control the airborne transmission diseases, such as COVID-19. To develop a flexible, robust, and low-costs tool for the simulation of polydisperse evaporating respiratory droplets, the Eulerian-Eulerian (E-E) approach is combined with the population balance equation (PBE). The former provides a highly efficient and low costs framework for the transport of the droplets and the interaction with the surrounding environment, while the latter is used to trace the dispersion and evaporation of the respiratory droplets. Two PBE solving methods, SM and QMOM, are adopted and compared on the basis of OpenFOAM and OpenQBMM. The developed solvers are verified and validated with experimental or numerical results concerning different aspects of respiratory droplets transport reported in literature.

The evaporation model and the thermal physical property models are verified first against the experimental results of a stationary evaporating droplet. The predicted droplet size time evolutions are in good agreement with the experimental data, which builds a solid foundation for the following coupled approaches.

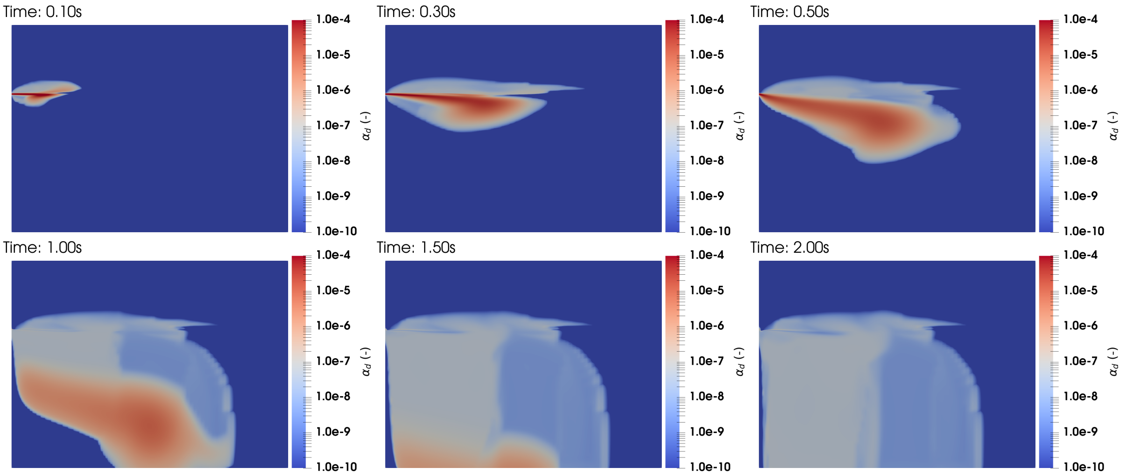

Figure 11: The disperse phase volume fraction α_d obtained by the QMOM poly-solver in symmetry plane at different times, from left to right and top to bottom: t=0.1, 0.3, 0.5, 1.0, 1.5 and 2.0 s.

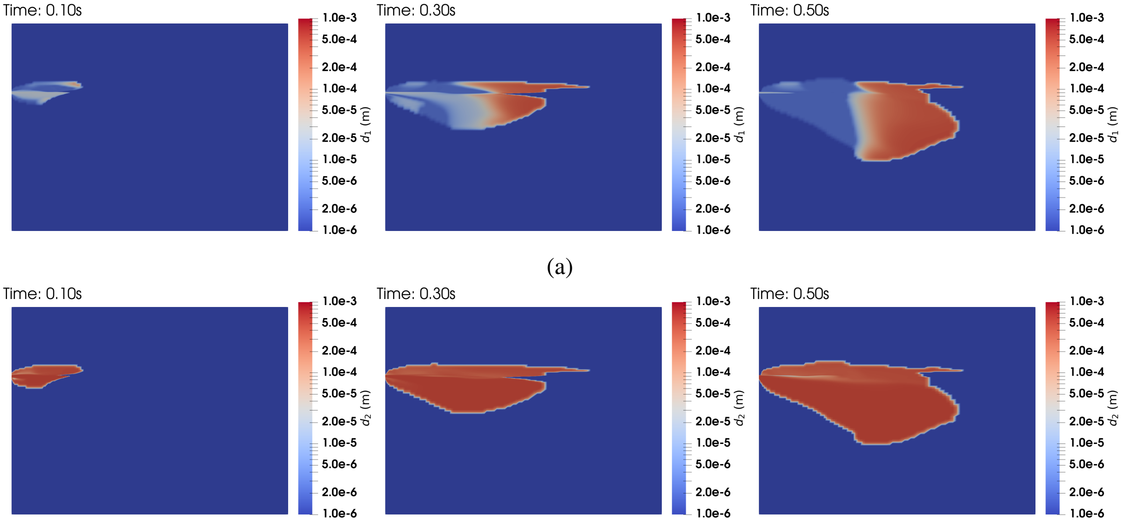

(a)

(b)

Figure 12: The quadrature node diameter obtained by the QMOM poly-solver in the symmetry plane at different times, from left to right: t=0.1, 0.3 and 0.5 s: (a) 1st quadrature node $d_{\mathrm{d},1}$, (b) 2nd quadrature node $d_{\mathrm{d},2}$.

The evaporation model is further validated with the reported diameter changes of evaporating droplets in literature. Both SM and QMOM agree well with literature, indicating that the CFD-PBE approach can be used to trace the droplets evaporation.

Since the respiratory droplets are carried by and interact with the expelled airflow, the ability of the CFD-PBE approach to accurately predict the evolution of the expelled airflow during respiratory activities is assessed. The poly-solver solving TFM and PBE is validated using the measured temporal evolution of the sneeze jet front. The simulation agrees well with the measurement. The transition from jet stage to puff stage is captured. Therefore, the solver can be used in the simulations of respiratory activities.

The reliability of the CFD-PBE approach is further tested by comparing the predicted results of the poly-solver with the experimental results for the aerosols transmission in a 3D chamber. It is found that both velocity profiles and concentration distributions agree well with the experimental results. The approach is reliable for aerosols transmission simulations.

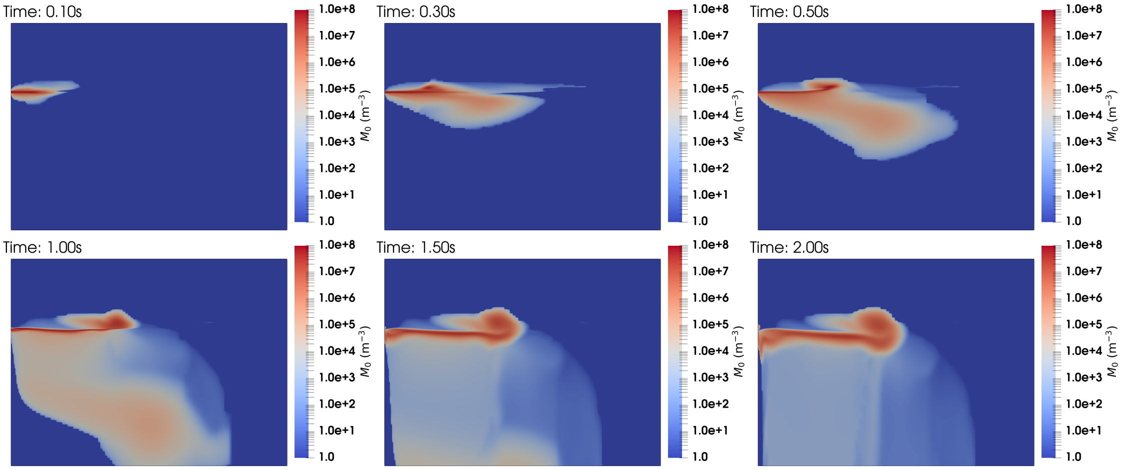

Figure 13: The 0th order moment M_0 obtained by the QMOM poly-solver in the symmetry plane at different times, from left to right and top to bottom: t=0.1, 0.3, 0.5, 1.0, 1.5 and 2.0 s.

Finally, the CFD-PBE approach is applied in the dispersion and evaporation of cough droplets in a 3D chamber. The SM-solver and poly-solver are adopted and compared. The evaporating and suspending trends of small droplets and the falling trends of the large droplets are presented by both approaches. The droplets are found to be able to travel a distance longer than 2 m, which is valuable for the guidelines of social distancing. Additionally, the advantages and disadvantages of the two methods are discussed. Both methods can directly provide variables, like volume fraction for analyses. Compared with SM, no manual intervention is required for QMOM, which is free of unreasonable results caused by inappropriate criteria.

Our future work will focus on the performance and computational costs evaluation of the developed CFD-PBE approach and its application in more complex and realistic scenarios, such as meeting room with ventilation systems and people. The effect of different ventilation systems on the trajectories of large droplets and the time of small droplets remaining in air will be investigated.

A. Algorithm for PBE with a single velocity

Eq. (30) is solved by a time-splitting method as following:

(1) Use the initial M_3 and M_2 to calculate the disperse phase diameter (Sauter mean diameter) d_d as in Eq. (33), with which update the interfacial models. Then, solve the TFM to obtain the disperse phase velocity $\mathbf{U}_\mathrm{d}$ and the interfacial mass transfer rate $\dot{m}$;

(2) Use $\mathbf{U}_\mathrm{d}$ obtained from TFM to solve the moment equations containing advection part as:

$$\frac{\partial M_k}{\partial t} + \nabla \cdot (\mathbf{U}_\mathrm{d} M_k) = 0, \tag{44}$$

and update the quadrature, w_p and d_p;

(3) Use $\dot{m}$ obtained from TFM to calculate $G_{\mathrm{d},p}$ and update the abscissas as:

$$d_p(t+\Delta t) = d_p(t) - \frac{2}{\rho_\mathrm{d} \pi d_p M_1} \dot{m} \Delta t. \tag{45}$$

If $d_p(t+\Delta t) < d_\mathrm{min}$, let $d_p(t+\Delta t) = d_\mathrm{min}$ to limit the minimum diameter of the droplets and $k_\mathrm{c} = 0$ to make $\dot{m}$ be consistent in TFM abd PBE. Finally, update the moments using the weights and the updated abscissas and return to step (1).

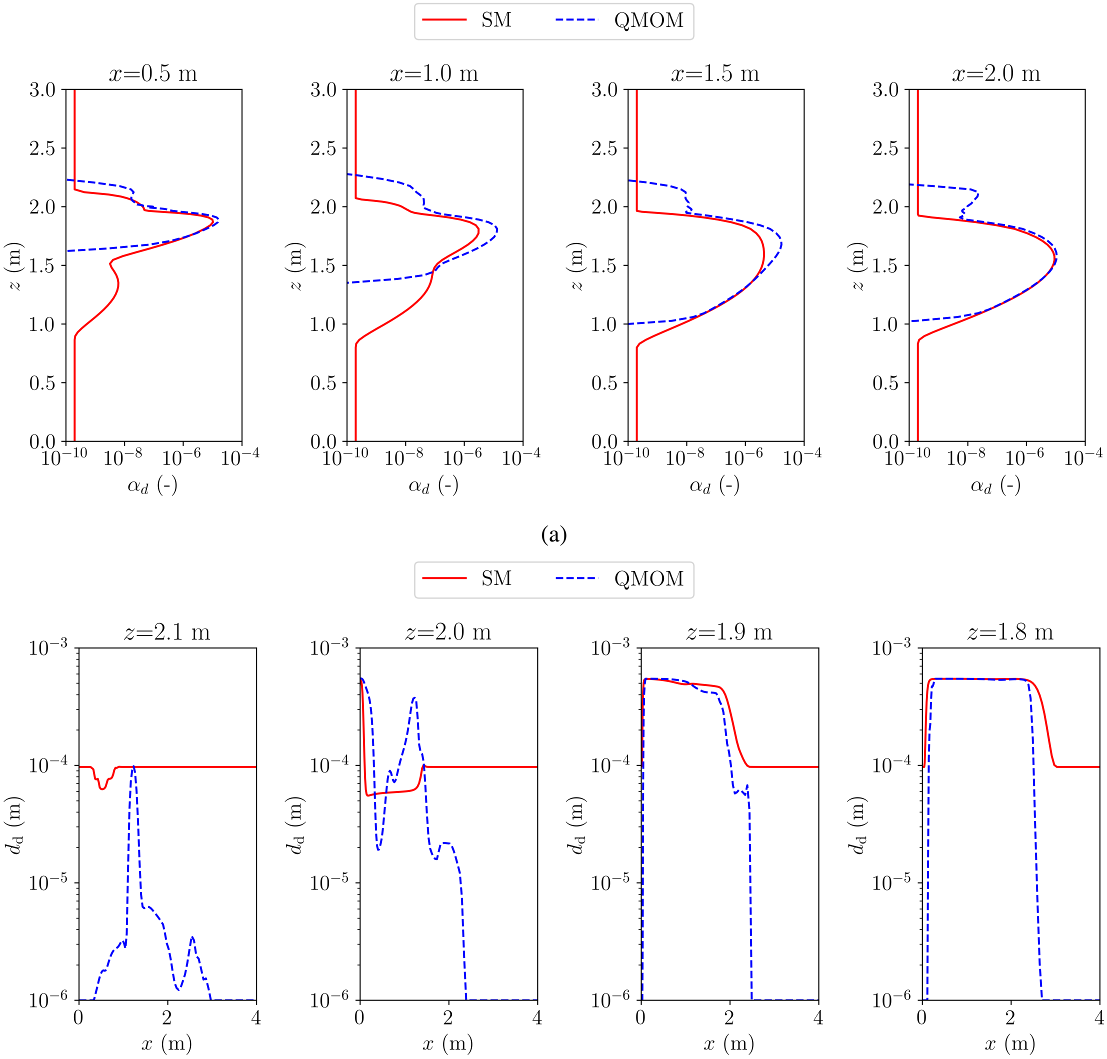

(a)

(b)

Figure 14: Comparison of the disperse phase variables obtained using SM and QMOM in the symmetry plane at t=0.5 s: (a) vertical distribution of the disperse phase volume fraction α_d at x=0.5, 1.0, 1.5 and 2.0 m, (b) horizontal distribution of the disperse phase diameter d_d at z= 2.1, 2.0, 1.9 and 1.8 m.

B. Algorithm for PBE with multiple velocities

Eq. (38) and Eq. (39) are also solved by a time-splitting method as in Heylmun et al. (2019):

(1) Use M_k and $\mathcal{U}_k$ to find w_p, d_p and $\mathbf{U}_p$. And calculate the relative velocity as $\mathbf{V}_p = \mathbf{U}_p - \mathbf{U}_\mathrm{d}$;

(2) Solve the relative transport equation to obtain M_k^* and $\mathcal{U}_k^*$ as:

$$\frac{\partial M_k}{\partial t} + \nabla \cdot \mathcal{V}_k = 0, \tag{46}$$

$$\frac{\partial \mathcal{U}_k}{\partial t} + \nabla \cdot \mathcal{P}_{k,r} = 0. \tag{47}$$

(3) Use M_k^* and $\mathcal{U}_k^*$ to update the quadrature node volume fraction and diameter as $\alpha_{\mathrm{d},p} = (\alpha_\mathrm{d} w_p d_p^3)/M_3$ and $d_{\mathrm{d},p} = d_p$. Then, solve the TFM to update the average disperse phase velocity $\mathbf{U}_\mathrm{d}$ and the interfacial mass transfer rate of the pth node $\dot{m}_p$;

(4) Correct the flux to make α_d consistent with $\frac{\pi}{6}M_3$ by solving the following equation of ψ

$$\frac{6\alpha_\mathrm{d}/\pi - M_3^*}{\Delta t} + \nabla\cdot(M_3^*\mathbf{U}_\mathrm{d}) + \nabla\cdot(M_3^*\nabla\psi) = 0, \tag{48}$$

then, the average velocity is corrected as $\mathbf{U}_\mathrm{d}^* = \mathbf{U}_\mathrm{d} + \nabla\psi$;

(5) Use $\mathbf{U}_\mathrm{d}^*$ to solve the average transport equation as

$$\frac{\partial M_k}{\partial t} + \nabla\cdot(M_k\mathbf{U}_\mathrm{d}^*) = 0, \tag{49}$$

$$\frac{\partial \mathcal{U}_k}{\partial t} + \nabla\cdot(\mathbf{U}_\mathrm{d}^*\otimes\mathcal{U}_k) = 0, \tag{50}$$

and updated w_p, d_p and $\mathbf{U}_p$;

(6) Use $\dot{m}_p$ obtained from TFM to update the size abscissas d_p as

$$d_p(t+\Delta t) = d_p(t) - \frac{2}{\rho_\mathrm{d}\pi w_p d_p^2}\dot{m}_p\Delta t, \tag{51}$$

If $d_p(t+\Delta t) < d_\mathrm{min}$, then let $d_p(t+\Delta t) = d_\mathrm{min}$ and $k_\mathrm{c} = 0$. Update the velocity abscissas $\mathbf{U}_p$ by solving the following equations:

$$\alpha_{\mathrm{d},p}\rho_\mathrm{d}\frac{\partial\mathbf{U}_p}{\partial t} = \alpha_{\mathrm{d},p}\rho_\mathrm{d}\mathbf{g} + \mathbf{M}_{\mathrm{d},p} - \dot{m}_p\mathbf{U}_p, \tag{52}$$

where $\mathbf{M}_{\mathrm{d},p}$ is the forces acted on the pth node, such as drag force;

(7) After updating $\mathbf{U}_p$, re-compute $\mathcal{U}_k$, and the mass averaged $\mathbf{U}_\mathrm{d}$ as

$$\mathbf{U}_\mathrm{d} = \frac{\sum_{p=0}^{N-1}\left(w_p d_p^3\mathbf{U}_p\right)}{M_3}, \tag{53}$$

and return to step (1) with updated M_k and $\mathcal{U}_k$.

C. Thermal physical properties

The thermal physical properties are of great importance in the simulation of droplet evaporation. For the present evaporation model, the following thermal physical variables are important: density, absolute enthalpy, sensible internal energy, heat capacity, dynamic viscosity and conductivity. Fortunately, OpenFOAM provides numerous thermal physical property models which can provide accurate descriptions of properties of the substances. For the disperse phase, the pure water droplets, the constant thermal physical properties for pure substance are adopted as: the density $\rho_\mathrm{d} = 1000\ \mathrm{kg\cdot m^{-3}}$, the heat capacity at constant volume $C_\mathrm{v,d} = 4195\ \mathrm{J\cdot kg^{-1}\cdot K^{-1}}$, the chemical enthalpy $H_\mathrm{c,d} = -1.5879\ \times 10^7\mathrm{J\cdot kg^{-1}}$, the dynamic viscosity $\mu_\mathrm{d} = 8.9266\times10^{-4}\ \mathrm{kg\cdot m^{-1}\cdot s^{-1}}$ and the Prandtl number $\mathrm{Pr} = 6.14$. Then, the absolute enthalpy is $H_\mathrm{a,d} = C_\mathrm{v,d}(T_\mathrm{d} - T^*) + H_\mathrm{c,d} + p/\rho_\mathrm{d}$, where $T^* = 298.15$ K is the reference temperature, the sensible internal energy is $E_\mathrm{d} = C_\mathrm{v,d}(T_\mathrm{d} - T^*)$ and the conductivity is $\kappa_\mathrm{d} = C_\mathrm{p,d}\mu_\mathrm{d}/\mathrm{Pr}$.

For the continuous phase, the thermal physical models for a two-component mixture (water vapor and air) are adopted. For each component, the absolute enthalpy and sensible internal energy are calculated by polynomials of temperature fitting NIST-JANAF thermalchemial tables as:

$$H_\mathrm{a} = R\left(\frac{a_4}{5}T^5 + \frac{a_3}{4}T^4 + \frac{a_2}{3}T^3 + \frac{a_1}{2}T^2 + a_0T + a_5\right), \tag{54}$$

$$E = H_{\mathrm{a}} - H_{\mathrm{a}}^{*} - p/\rho_{\mathrm{c}}, \tag{55}$$

where R is the specific gas constant, a_i are the coefficients and listed in Table 6, and $H_{\mathrm{a},}^{*}$ is the reference enthalpy equal to the absolute enthalpy at T^* (298.15 K). The viscosity and conductivity are specified by Sutherland's law as:

$$\mu = \frac{A_{\mathrm{s}}\sqrt{T}}{1 + T_{\mathrm{s}}/T}, \tag{56}$$

$$\kappa = \mu C_{\mathrm{v}}(1.32 + 1.77R/C_{\mathrm{v}}), \tag{57}$$

where $A_{\mathrm{s}} = 1.458 \times 10^{-6}$ and $T_{\mathrm{s}} = 110.4$ for both components.

Finally, the variable ϕ for the mixture is calculated by the specie mass fraction Y_i and variable ϕ_i as $\phi = \sum_i^2 Y_i\phi_i$. Additionally, the molar mass for air is $W_{\mathrm{air}} = 28.96\ \mathrm{kg \cdot kmol^{-1}}$, for water vapor is $M_{\mathrm{water}} = 18.02\ \mathrm{kg \cdot kmol^{-1}}$ and for the mixture is $\bar{M} = 1/(\sum_i^2 Y_i/M_i)$. The density of the mixture is calculated by the perfect gas equation.

Table 6
Coefficients for thermal properties of water vapor and air.

specie	a_0	a_1	a_2	a_3	a_4	a_5
Water vapor	4.19864	-0.00203643	6.5204e-06	-5.48797e-09	1.77198e-12	-30293.7
Air	3.09589	1.22835e-03	-4.14267e-07	6.56910e-11	-3.87021e-15	-983.191

D. Grid convergence examination

The grid convergence is examined using three grids having 364640 (coarse), 831220 (middle) and 1912700 (fine) cube cells, respectively. The grid is refined in the three directions with a factor of approximately 1.3, so the total factor is about 2.3. The case of sneeze jet front evolution in section 3.3 is adopted for the grid convergence examination. The results are shown in Figure 15. It can be seen that differences in the results of the three grids are small. However, the result of coarse grid shows a step-function like behavior after $t = 0.6$ s. For example, the moving distance of the jet front keeps 1.28 m from 0.9 s to 1.0 s and then increases to 1.33 m and keeps constant from 1.05 s to 1.15 s. This is because after $t = 0.6$ s, the velocity of the exhaled jet (or puff) is low. The coarse grid is difficult to capture the slow movement. However, the middle and the fine grid, showing a continuously increment, can better capture such a slow movement. Considering the computational costs and accuracy, the middle grid of 831220 cells is adopted for the simulations in this study.

References

Balachandar, S., Zaleski, S., Soldati, A., Ahmadi, G., Bourouiba, L., 2020. Host-to-host airborne transmission as a multiphase flow problem for science-based social distance guidelines. Int. J. Multiph. Flow 132, 103439. doi:`10.1016/j.ijmultiphaseflow.2020.103439`.

Burgmann, S., Janoske, U., 2021. Transmission and reduction of aerosols in classrooms using air purifier systems. Phys. Fluids 33, 033321. doi:`10.1063/5.0044046`.

Capecelatro, J., Desjardins, O., 2013. An Euler–Lagrange strategy for simulating particle-laden flows. J. Comput. Phys. 238, 1–31. doi:`10.1016/j.jcp.2012.12.015`.

Chao, C., Wan, M., Morawska, L., Johnson, G., Ristovski, Z., Hargreaves, M., Mengersen, K., Corbett, S., Li, Y., Xie, X., Katoshevski, D., 2009. Characterization of expiration air jets and droplet size distributions immediately at the mouth opening. Journal of Aerosol Science 40, 122–133. doi:`10.1016/j.jaerosci.2008.10.003`.

Chen, F., Yu, S.C., Lai, A.C., 2006. Modeling particle distribution and deposition in indoor environments with a new drift–flux model. Atmospheric Environment 40, 357–367. doi:`10.1016/j.atmosenv.2005.09.044`.

Chong, K.L., Ng, C.S., Hori, N., Yang, R., Verzicco, R., Lohse, D., 2021. Extended Lifetime of Respiratory Droplets in a Turbulent Vapor Puff and Its Implications on Airborne Disease Transmission. Phys. Rev. Lett. 126, 034502. doi:`10.1103/PhysRevLett.126.034502`.

Coldrick, S., Kelsey, A., Ivings, M.J., Foat, T.G., Parker, S.T., Noakes, C.J., Bennett, A., Rickard, H., Moore, G., 2022. Modeling and experimental study of dispersion and deposition of respiratory emissions with implications for disease transmission. Indoor Air 32. doi:`10.1111/ina.13000`.

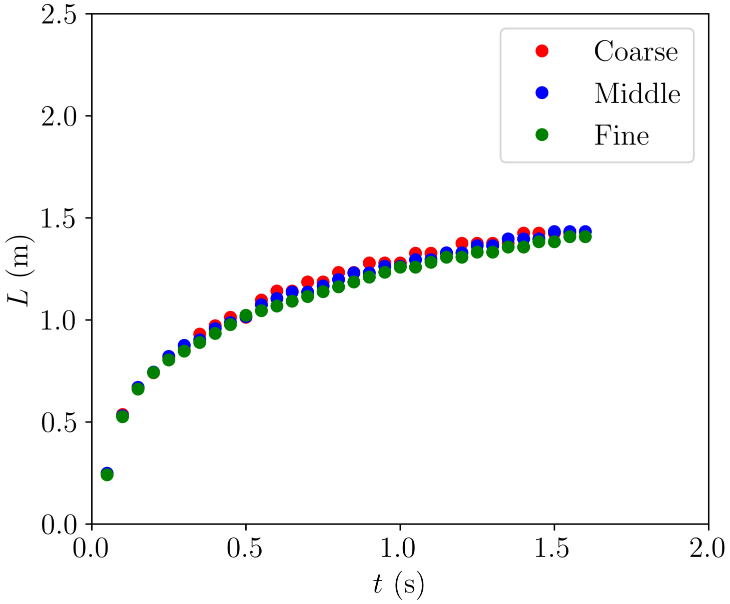

Figure 15: The results of grid convergence examination.

Dalla Barba, F., Wang, J., Picano, F., 2021. Revisiting D 2-law for the evaporation of dilute droplets. Physics of Fluids 33, 051701. doi:`10.1063/5.0051078`.

Dbouk, T., Drikakis, D., 2020. On coughing and airborne droplet transmission to humans. Phys. Fluids 32, 053310. doi:`10.1063/5.0011960`.

Diwan, S.S., Ravichandran, S., Govindarajan, R., Narasimha, R., 2020. Understanding Transmission Dynamics of COVID-19-Type Infections by Direct Numerical Simulations of Cough/Sneeze Flows. Trans. Indian Natl. Acad. Eng. 5, 255–261. doi:`10.1007/s41403-020-00106-w`.

ESI-OpenCFD, 2021. ESI OpenCFD Release OpenFOAM® v2106. https://www.openfoam.com/news/main-news/openfoam-v2106.

Fabregat, A., Gisbert, F., Vernet, A., Dutta, S., Mittal, K., Pallarès, J., 2021a. Direct numerical simulation of the turbulent flow generated during a violent expiratory event. Phys. Fluids 33, 035122. doi:`10.1063/5.0042086`.

Fabregat, A., Gisbert, F., Vernet, A., Ferré, J.A., Mittal, K., Dutta, S., Pallarès, J., 2021b. Direct numerical simulation of turbulent dispersion of evaporative aerosol clouds produced by an intense expiratory event. Physics of Fluids 33, 033329. doi:`10.1063/5.0045416`.

Faeth, G., 1979. Current status of droplet and liquid combustion, in: Energy and Combustion Science. Elsevier, pp. 149–182. doi:`10.1016/B978-0-08-024780-9.50013-7`.

Feng, Y., 2020. Influence of wind and relative humidity on the social distancing effectiveness to prevent COVID-19 airborne transmission: A numerical study. J. Aerosol Sci. , 19doi:`10.1016/j.jaerosci.2020.105585`.

Frössling, N., 1938. On the vaporization of a falling drop. Gerlands Beitr. Geophys. 52, 170–216.

Garg, R., Narayanan, C., Subramaniam, S., 2009. A numerically convergent Lagrangian–Eulerian simulation method for dispersed two-phase flows. Int. J. Multiph. Flow 35, 376–388. doi:`10.1016/j.ijmultiphaseflow.2008.12.004`.

Gupta, J.K., Lin, C.H., Chen, Q., 2009. Flow dynamics and characterization of a cough: Flow dynamics and characterization of a cough. Indoor Air 19, 517–525. doi:`10.1111/j.1600-0668.2009.00619.x`.

He, R., Liu, W., Elson, J., Vogt, R., Maranville, C., Hong, J., 2021. Airborne transmission of COVID-19 and mitigation using box fan air cleaners in a poorly ventilated classroom. Phys. Fluids 33, 057107. doi:`10.1063/5.0050058`.

Heylmun, J., Kong, B., Passalacqua, A., Fox, R., 2019. A quadrature-based moment method for polydisperse bubbly flows. Comput. Phys. Commun. 244, 187–204. doi:`10.1016/j.cpc.2019.06.005`.

Huang, L., Riyadi, S., Utama, I., Li, M., Sun, P., Thomas, G., 2022. COVID-19 transmission inside a small passenger vessel: Risks and mitigation. Ocean Eng. 255, 111486. doi:`10.1016/j.oceaneng.2022.111486`.

Lehnigk, R., Bainbridge, W., Liao, Y., Lucas, D., Niemi, T., Peltola, J., Schlegel, F., 2022. An open-source population balance modeling framework for the simulation of polydisperse multiphase flows. AIChE J. 68. doi:`10.1002/aic.17539`.

Li, H., Leong, F.Y., Xu, G., Ge, Z., Kang, C.W., Lim, K.H., 2020. Dispersion of evaporating cough droplets in tropical outdoor environment. Phys. Fluids 32, 113301. doi:`10.1063/5.0026360`.

Li, X., Shang, Y., Yan, Y., Yang, L., Tu, J., 2018. Modelling of evaporation of cough droplets in inhomogeneous humidity fields using the multi-component Eulerian-Lagrangian approach. Build. Environ. 128, 68–76. doi:`10.1016/j.buildenv.2017.11.025`.

Li, X., Yan, Y., Shang, Y., Tu, J., 2015. An Eulerian–Eulerian model for particulate matter transport in indoor spaces. Build. Environ. 86, 191–202. doi:`10.1016/j.buildenv.2015.01.010`.

Li, Z., Zhang, X., Wu, T., Zhu, L., Qin, J., Yang, X., 2021. Effects of slope and speed of escalator on the dispersion of cough-generated droplets from a passenger. Phys. Fluids 33, 041701. doi:`10.1063/5.0046870`.

Lieber, C., Melekidis, S., Koch, R., Bauer, H.J., 2021. Insights into the evaporation characteristics of saliva droplets and aerosols: Levitation experiments and numerical modeling. J. Aerosol Sci. 154, 105760. doi:`10.1016/j.jaerosci.2021.105760`.

Liu, H., He, S., Shen, L., Hong, J., 2021. Simulation-based study of COVID-19 outbreak associated with air-conditioning in a restaurant. Phys. Fluids 33, 023301. doi:`10.1063/5.0040188`.

Liu, J., Duan, Y., 2012. Saliva: A potential media for disease diagnostics and monitoring. Oral Oncol. 48, 569–577. doi:`10.1016/j.oraloncology.2012.01.021`.

Marchisio, D.L., Fox, R.O., 2013. Computational Models for Polydisperse Particulate and Multiphase Systems. Cambridge Series in Chemical Engineering, Cambridge University Press, Cambridge. doi:`10.1017/CBO9781139016599`.

Mirikar, D., Palanivel, S., Arumuru, V., 2021. Droplet fate, efficacy of face mask, and transmission of virus-laden droplets inside a conference room. Phys. Fluids 33, 065108. doi:`10.1063/5.0054110`.

Mittal, R., Ni, R., Seo, J.H., 2020. The flow physics of COVID-19. J. Fluid Mech. 894, F2. doi:`10.1017/jfm.2020.330`.

Motamedi, H., Shirzadi, M., Tominaga, Y., Mirzaei, P.A., 2022. CFD modeling of airborne pathogen transmission of COVID-19 in confined spaces under different ventilation strategies. Sustain. Cities Soc. 76, 103397. doi:`10.1016/j.scs.2021.103397`.

Ooi, C.C., Suwardi, A., Ou Yang, Z.L., Xu, G., Tan, C.K.I., Daniel, D., Li, H., Ge, Z., Leong, F.Y., Marimuthu, K., Ng, O.T., Lim, S.B., Lim, P., Mak, W.S., Cheong, W.C.D., Loh, X.J., Kang, C.W., Lim, K.H., 2021. Risk assessment of airborne COVID-19 exposure in social settings. Phys. Fluids 33, 087118. doi:`10.1063/5.0055547`.

OpenFOAM-Foundation, 2020. OpenFOAM 8 Released. https://openfoam.org/release/8/.

Passalacqua, A., Heylmun, J., Icardi, M., Madadi, E., Bachant, P., Hu, X., Weaver, J., 2021. OpenQBMM/OpenQBMM: OpenQBMM 7.0.0 for OpenFOAM v2106. Zenodo. doi:`10.5281/ZENODO.5039574`.

Pei, G., Taylor, M., Rim, D., 2021. Human exposure to respiratory aerosols in a ventilated room: Effects of ventilation condition, emission mode, and social distancing. Sustain. Cities Soc. 73, 103090. doi:`10.1016/j.scs.2021.103090`.

Ranz, W., Marshall, W., 1952a. Evaporation from drops. Part I. Chem. Eng. Prog. 48, 141–146.

Ranz, W., Marshall, W., 1952b. Evaporation from drops. Part II. Chem. Eng. Prog. 48, 173–180.

Redrow, J., Mao, S., Celik, I., Posada, J.A., Feng, Z.g., 2011. Modeling the evaporation and dispersion of airborne sputum droplets expelled from a human cough. Build. Environ. 46, 2042–2051. doi:`10.1016/j.buildenv.2011.04.011`.

Rosti, M.E., Cavaiola, M., Olivieri, S., Seminara, A., Mazzino, A., 2021. Turbulence role in the fate of virus-containing droplets in violent expiratory events. Phys. Rev. Res. 3, 013091. doi:`10.1103/PhysRevResearch.3.013091`.

Rosti, M.E., Olivieri, S., Cavaiola, M., Seminara, A., Mazzino, A., 2020. Fluid dynamics of COVID-19 airborne infection suggests urgent data for a scientific design of social distancing. Sci. Rep. 10, 22426. doi:`10.1038/s41598-020-80078-7`.

Salman, H., Soteriou, M., 2004. Lagrangian simulation of evaporating droplet sprays. Phys. Fluids 16, 4601–4622. doi:`10.1063/1.1809132`.

Schiller, L., Naumann, A., 1933. A Drag Coefficient Correlation. Z. Ver. Dtsch. Ingenieure 77, 318–320.

Sen, N., 2021. Transmission and evaporation of cough droplets in an elevator: Numerical simulations of some possible scenarios. Phys. Fluids 33, 033311. doi:`10.1063/5.0039559`.

Shiea, M., Buffo, A., Vanni, M., Marchisio, D., 2020. Numerical Methods for the Solution of Population Balance Equations Coupled with Computational Fluid Dynamics. Annu. Rev. Chem. Biomol. Eng. 11, 339–366. doi:`10.1146/annurev-chembioeng-092319-075814`.

Singhal, R., Ravichandran, S., Diwan, S.S., 2021. Direct Numerical Simulation of a Moist Cough Flow using Eulerian Approximation for Liquid Droplets. Int. J. Comput. Fluid Dyn. 35, 778–797. doi:`10.1080/10618562.2022.2057479`.

Singhal, R., Ravichandran, S., Govindarajan, R., Diwan, S.S., 2022. Virus transmission by aerosol transport during short conversations. Flow 2, E13. doi:`10.1017/flo.2022.7`.

Stiehl, B., Shrestha, R., Schroeder, S., Delgado, J., Bazzi, A., Reyes, J., Kinzel, M., Ahmed, K., 2022. The effect of relative air humidity on the evaporation timescales of a human sneeze. AIP Adv. 12, 075210. doi:`10.1063/5.0102078`.

Talaat, K., Abuhegazy, M., Mahfoze, O.A., Anderoglu, O., Poroseva, S.V., 2021. Simulation of aerosol transmission on a Boeing 737 airplane with intervention measures for COVID-19 mitigation. Phys. Fluids 33, 033312. doi:`10.1063/5.0044720`.

Wang, H., Li, Z., Liu, Y., Zhu, L., Zhou, Z., 2022a. Experimental study of the dispersion of cough-generated droplets from a person going up- or downstairs. AIP Adv. 12, 015002. doi:`10.1063/5.0073880`.

Wang, J., Alipour, M., Soligo, G., Roccon, A., De Paoli, M., Picano, F., Soldati, A., 2021a. Short-range exposure to airborne virus transmission and current guidelines. Proc. Natl. Acad. Sci. 118, e2105279118. doi:`10.1073/pnas.2105279118`.

Wang, J., Dalla Barba, F., Picano, F., 2021b. Direct numerical simulation of an evaporating turbulent diluted jet-spray at moderate reynolds number. Int. J. Multiph. Flow 137, 103567. doi:`10.1016/j.ijmultiphaseflow.2021.103567`.

Wang, Z., Galea, E.R., Grandison, A., Ewer, J., Jia, F., 2022b. A coupled Computational Fluid Dynamics and Wells-Riley model to predict COVID-19 infection probability for passengers on long-distance trains. Saf. Sci. 147, 105572. doi:`10.1016/j.ssci.2021.105572`.

Wei, J., Li, Y., 2015. Enhanced spread of expiratory droplets by turbulence in a cough jet. Build. Environ. 93, 86–96. doi:`10.1016/j.buildenv.2015.06.018`.

Wells, W.F., 1934. On air-borne infections: Study II. Droplets and droplet nuclei. Am. J. Epidemiol. 20, 611–618. doi:`10.1093/oxfordjournals.aje.a118097`.

WHO, 2020. Transmission of SARS-CoV-2: Implications for Infection Prevention Precautions. Technical Report.

Yan, Y., Fang, X., Li, X., Tao, Y., Yan, P., Tu, J., 2022. Evaporation flow characteristics of respiratory droplets: Dynamic property under multifarious ambient conditions. Build. Environ. 221, 109272. doi:`10.1016/j.buildenv.2022.109272`.

Yan, Y., Li, X., Ito, K., 2020. Numerical investigation of indoor particulate contaminant transport using the Eulerian-Eulerian and Eulerian-Lagrangian two-phase flow models. Exp. Comput. Multiph. Flow 2, 31–40. doi:`10.1007/s42757-019-0016-z`.

Yan, Y., Li, X., Tu, J., 2019. Thermal effect of human body on cough droplets evaporation and dispersion in an enclosed space. Build. Environ. 148, 96–106. doi:`10.1016/j.buildenv.2018.10.039`.

Yang, Y., Wang, Y., Su, C., Liu, X., Yuan, X., Chen, Z., 2022. Numerical Investigation on the Droplet Dispersion inside a Bus and the Infection Risk Prediction. Appl. Sci. 12, 5909. doi:10.3390/app12125909.

Yuan, C., Laurent, F., Fox, R., 2012. An extended quadrature method of moments for population balance equations. J. Aerosol Sci. 51, 1–23. doi:10.1016/j.jaerosci.2012.04.003.

Zhang, Z., Chen, Q., 2007. Comparison of the Eulerian and Lagrangian methods for predicting particle transport in enclosed spaces. Atmos. Environ. 41, 5236–5248. doi:10.1016/j.atmosenv.2006.05.086.

Zhang, Z., Han, T., Yoo, K.H., Capecelatro, J., Maki, K., 2021. Disease transmission through expiratory aerosols on an urban bus. Phys. Fluids 33, 015116. doi:10.1063/5.0037452.

Zhao, B., Yang, C., Yang, X., Liu, S., 2008. Particle dispersion and deposition in ventilated rooms: Testing and evaluation of different Eulerian and Lagrangian models. Build. Environ. 43, 388–397. doi:10.1016/j.buildenv.2007.01.005.

Zhu, S., Kato, S., Yang, J.H., 2006. Study on transport characteristics of saliva droplets produced by coughing in a calm indoor environment. Build. Environ. 41, 1691–1702. doi:10.1016/j.buildenv.2005.06.024.